RESEARCH ARTICLE

A Novel Inversion Approach for the Kernel-Driven BRDF Model for Heterogeneous Pixels

Hanliang Li[1], Kai Yan[1,2*], Si Gao[2], Xuanlong Ma[3], Yelu Zeng[4], Wenjuan Li[5,6], Gaofei Yin[7], Xihan Mu[1], Guangjian Yan[1], and Ranga B. Myneni[8]

[1]State Key Laboratory of Remote Sensing Science, Faculty of Geographical Science, Beijing Normal University, Beijing 100875, China. [2]School of Land Science and Technology, China University of Geosciences, Beijing 100083, China. [3]College of Earth and Environmental Sciences, Lanzhou University, Lanzhou 730020, China. [4]College of Land Science and Technology, China Agricultural University, Beijing 100083, China. [5]State Key Laboratory of Efficient Utilization of Arid and Semi-arid Arable Land in Northern China, the Institute of Agricultural Resources and Regional Planning, Chinese Academy of Agricultural Sciences, Beijing 100081, China. [6]INRAE, Avignon Université, UMR EMMAH, Avignon F-84000, France. [7]Faculty of Geosciences and Environmental Engineering, Southwest Jiaotong University, Chengdu 610031, China. [8]Department of Earth and Environment, Boston University, Boston, MA 02215, USA.

*Address correspondence to: kaiyan@cugb.edu.cn

The bidirectional reflectance distribution function (BRDF) of the land surface contains information relating to its physical structure and composition. Accurate BRDF modeling for heterogeneous pixels is important for global ecosystem monitoring and radiation balance studies. However, the original kernel-driven models, which many operational BRDF/Albedo algorithms have adopted, do not explicitly consider the heterogeneity within heterogeneous pixels, which may result in large fitting residuals. In this paper, we attempted to improve the fitting ability of the kernel-driven models over heterogeneous pixels by changing the inversion approach and proposed a dynamic weighted least squares (DWLS) inversion approach. The performance of DWLS and the traditional ordinary least squares (OLS) inversion approach were compared using simulated data. We also evaluated its ability to reconstruct multiangle satellite observations and provide accurate BRDF using unmanned aerial vehicle observations. The results show that the developed DWLS approach improves the accuracy of modeled BRDF of heterogeneous pixels. The DWLS approach applied to satellite observations shows better performance than the OLS method in study regions and exhibits smaller mean fitting residuals both in the red and near-infrared bands. The DWLS approach also shows higher BRDF modeling accuracy than the OLS approach with unmanned aerial vehicle observations. These results indicate that the DWLS inversion approach can be a better choice when kernel-driven models are used for heterogeneous pixels.

Introduction

The key to interpreting land surface characteristics by optical remote sensing is calculating the surface bidirectional reflectance distribution function (BRDF), which is usually used to quantify surface reflectance anisotropy in remote sensing [1,2]. Accurate BRDF modeling of the land surface can be used to correct the bidirectional effects in reflectance and to estimate land surface physical, biological, and vegetation structural parameters, such as albedo and leaf area index [3–6]. However, the accuracy of BRDF modeling is affected by spatial heterogeneity within the pixel [7–10]. Spatial heterogeneity generally originates from complex terrain and the mixture of different land cover types. The pixels with these heterogeneous factors are usually deemed heterogeneous pixels, which are common in moderate- and low-resolution satellite images [11,12].

Therefore, accurate BRDF modeling for heterogeneous pixels is important for global ecosystem monitoring and radiation balance studies.

Scholars have developed several empirical, semiempirical, and physical methods for BRDF modeling [13–17]. Among them, the semiempirical linear kernel-driven models originally proposed by Roujean et al. [18] have been widely used due to their simple forms and strong fitting ability. These kernel-driven models can use multiangle reflectance data to estimate the surface BRDF by a semiempirical linear fitting. Wanner et al. [19] and Lucht et al. [20] subsequently made them easier to understand and apply as the Algorithm for Model Bidirectional Reflectance Anisotropies of the Land Surface (AMBRALS) [21]. Many satellite sensors have used the kernel-driven models to generate land surface BRDF/Albedo products, including the Moderate Resolution Imaging Spectroradiometer (MODIS)

and Polarization and Directionality of the Earth's Reflectances (POLDER) [20,22–27]. The kernels are critical to the physical constraints of the kernel-driven models, which can provide possible BRDF shapes in unobserved regions of the viewing and illumination hemisphere. Many kernels have been developed to describe the radiative transfer or geometric-optical processes for different scenes, such as the well-known Roujean, RossThin, RossThick, LiSparse, and LiDense kernels [18–20,28]. The LiTransit kernel was also developed to better describe the geometric-optical relationships of discrete canopies under large zenith angles [28,29]. Meanwhile, the original kernel-driven models underestimate the hotspot effect. To address this problem, Maignan et al. [30] and Jiao et al. [31–33] further modified it by introducing the hotspot factors. After more than 20 years of development, kernel-driven models are used in many fields [34,35]. The reliability of these models was validated using multiangle observations and field measurements [36–38]. However, the original kernel-driven models do not explicitly consider the effect of subpixel heterogeneity and may lead to large fitting residuals in BRDF modeling [39,40].

Several methods based on kernel-driven models have been developed to improve the fitting ability for complex terrain or mixed land covers. Wu et al. [41] developed a new kernel-driven model for slope terrain based on the framework of the RossThick-LiSparseReciprocal (RTLSR) model. The new model has been shown to simulate the bidirectional reflectance factor (BRF) of the single slope more accurately. However, there are generally more complex composite slopes in the pixels of many moderate- and low-resolution sensors, such as MODIS (500 m × 500 m) and POLDER (6 km × 7 km). For this issue, Hao et al. [42] further developed an improved topography-coupled kernel-driven model, which can consider the effects of terrain and diffuse skylight using a digital elevation model (DEM) and sun-sensor geometry information. Then, an adaptive terrain algorithm that combines 2 kernel-driven models, called the topographic kernel-driven (Topo-KD), was developed by Yan et al. [40]. It can further consider multiple scattering effects caused by adjacent terrain. Kizel and Vidro [43] proposed a preliminary BRDF inversion approach based on the kernel-driven models to correct the undesired effects of mixed land cover pixels. These models all consider more explicitly the heterogeneity within the pixel by improving kernels of the kernel-driven model based on physical methods. Therefore, they all need to introduce additional auxiliary data or parameters, such as a DEM [40–42], and land cover maps [43], etc. These methods based on the physical theory improve the modeling accuracy of the kernel-driven model for heterogeneous pixels but also inevitably introduce additional input uncertainties that limit their large-scale applications. Currently, there is no method to improve the performance of the kernel-driven models on heterogeneous pixels by changing the inversion approach.

The objective of this paper is to improve the fitting ability of the kernel-driven model over heterogeneous pixels by using a new inversion approach. The dynamic weighted least squares (DWLS) inversion approach was proposed in this study, which is more suitable for heterogeneous pixels than the traditional ordinary least squares (OLS) inversion approach. This paper provides a comprehensive evaluation and analysis of the DWLS approach and is organized as follows. Materials describes the simulated, satellite, and unmanned aerial vehicle (UAV) data. Methods describes the details of the DWLS and OLS inversion approaches of the kernel-driven models. In Results, we compared

the performance of DWLS and OLS inversion approaches for satellite observation reconstruction and BRDF construction using UAV observations. The uncertainty of the DWLS approach was also analyzed in this section. The discussion and conclusions are presented in Discussion and Conclusion, respectively.

Materials

Simulated data

Obtaining ideal multiangle measurements over heterogeneous pixels is challenging. Computer simulation models provide a practical and feasible alternative to evaluate the DWLS approach. In this study, we employed the LargE-Scale remote sensing data and image Simulation framework (LESS) to assemble a reference dataset composed of simulated anisotropic reflectance data over heterogeneous pixels. LESS is a newly proposed ray-tracing-based 3-dimensional (3-D) radiative transfer model that can accurately and efficiently simulate multispectral and multiangle images and radiation properties of complex realistic landscapes [44,45]. The accuracy of the LESS model has been validated in comparison with other models (e.g., FLIGHT [46] and RAYTYAN [47]) over several different homogeneous and heterogeneous canopies from the Radiation transfer Model Intercomparison experiment, and also validated with published field measurement datasets [48,49]. The comparison results show that the LESS model has good simulation accuracy and can be used for approach validation [45]. The inputs for the LESS model include scene size, 3-D structure, component spectrum (e.g., leaf reflectance), sun-sensor geometry, and illumination parameters (e.g., skylight proportion) of the scene. The LESS model can simulate the radiative transfer process (absorption, reflection, and transmission) of incident light in a scene based on the ray-tracing strategy and output the corresponding simulated variables (such as BRF, albedo, and so on) [50]. Further detailed information on the LESS model can be found on the website (http://lessrt.org/).

Spatial heterogeneity generally originates from complex terrain and the mixture of different land cover types. We used the LESS model to evaluate the performance of the DWLS approach over rugged (complex terrain) and mixed (mixture of different land cover types) scenes, respectively. We selected the DEM of a 5.4-km × 5.4-km mountainous area (29.5°N, 98.1°E) as the terrain for the simulated pixels. The topographical conditions of the area are shown in Fig. 1. The area was divided into 25 pixels and used to simulate multiangle reflectance data. We also designed 4 mixed pixels and 1 control pixel to evaluate the DWLS approach (Fig. 2). The 4 mixed pixels can be seen as a mixture of 2 land cover types, forest and barren land. Instead, the trees are randomly distributed in the whole control pixel and can be seen as a forest pixel. The critical parameters of this simulation experiment are shown in Table 1. Soil was treated as a Lambertian in all simulation experiments.

MODIS data

In this paper, MODIS data were used to compare the performance of OLS and DWLS approaches in the reconstruction of missing satellite observations. The MODIS Collection 6 Terra/Aqua Surface Reflectance Daily L2G Global 500-m product provides daily surface BRF data at a gridded 500-m spatial resolution and for 7 spectral bands [51]. In this study, the red and near-infrared (NIR) bands (cantered at 648 and 858 nm, respectively) were used. By considering the 1-km data state quality
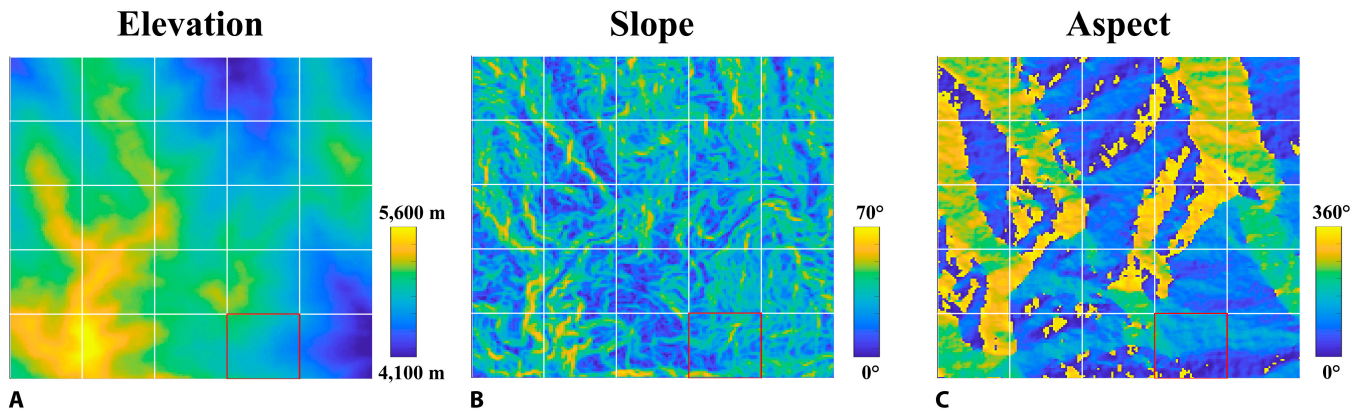
Fig. 1. Topographic conditions of the rugged area for simulation. (A) Elevation of the mountainous region. (B and C) Slope and aspect distribution, respectively. The pixel with the red line was used to compare the BRDF shapes inverted by the OLS and DWLS approaches in Fig. 7. The DEM is from the Advanced Spaceborne Thermal Emission and Reflection Radiometer global DEM version 2 (https://lpdaac.usgs.gov/).
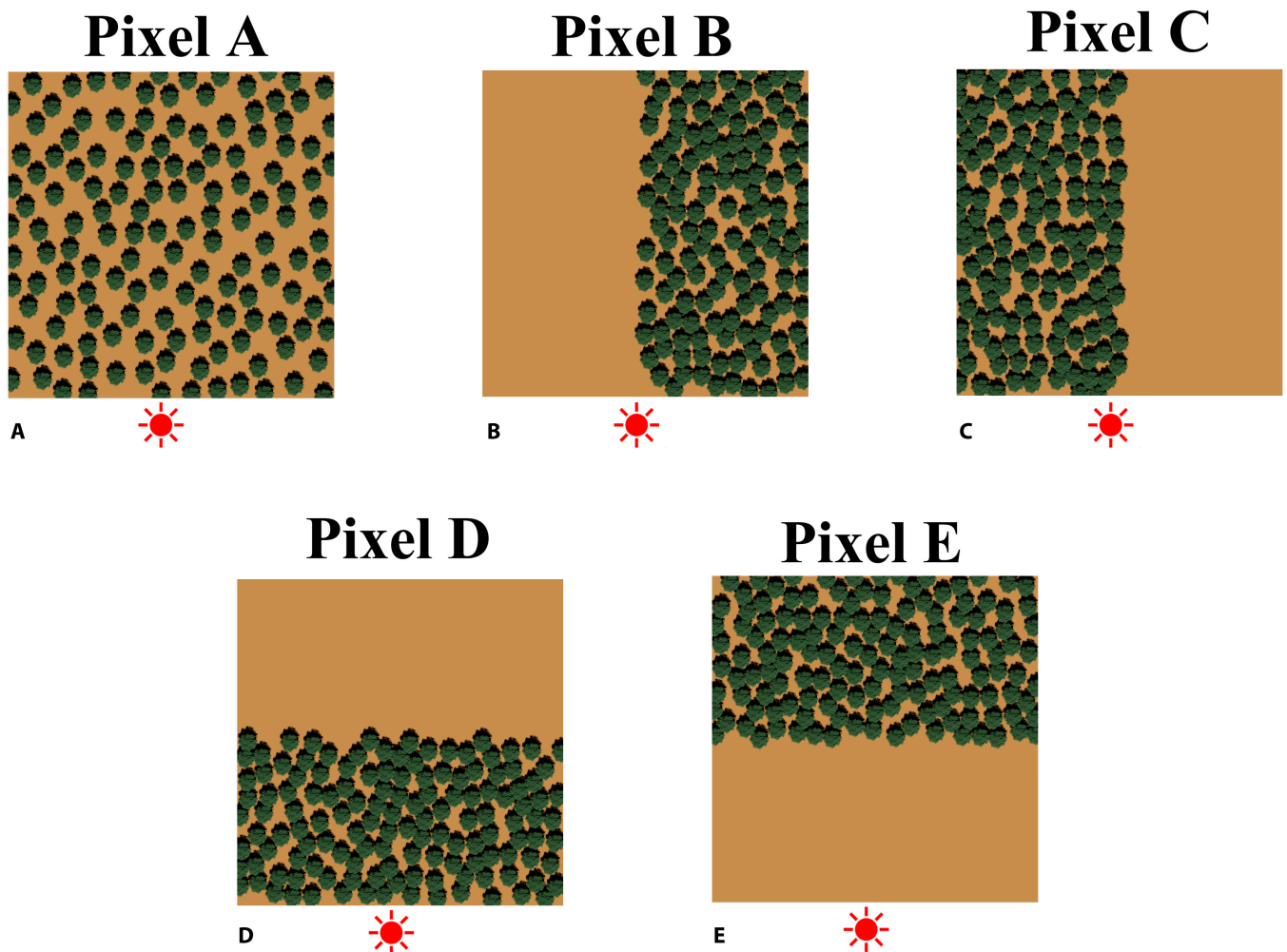

Fig. 2. The scenes of a control pixel (A) and 4 mixed pixels (B to E) for evaluation of the DWLS approach.

assurance and the 500-m quality control, we extracted the gridded 500-m multiangle observations for 16 d and synthesized a multiangle observation dataset from the MOD09GA and MYD09GA reflectance products. The reflectance characteristics were assumed to be stable during the period. Table 2 lists the

thresholds used to control the quality of this dataset. Two regions were selected as the validation area to test the ability of the DWLS approach in reconstructing the observations: (a) a 40-km × 40-km region (80 × 80 pixels) located in Africa (22°0′56″ to 22°24′29″E, 14°16′37″ to 14°37′13″S); (b) a

Table 1. Critical parameters of the simulation experiment.

Parameters		Experiment settings
Solar	Zenith angle	0°/15°/30°/45°/60°
	Azimuth angle	150°/180°/210°
Sensor	Zenith angle	0°:5°:60° [a]
	Azimuth angle	0°:30°:330°
Component spectra	Leaf	Reflectance: 0.0546 (red) / 0.4957 (NIR) [b]
		Transmittance: 0.0149 (red) / 0.4409 (NIR)
	Soil	Reflectance: 0.1270 (red) / 0.1590 (NIR)
		Transmittance: 0 (red) / 0 (NIR)

[a]*a*:*b*:*c* indicate that the range of value is *a* to *c* with an increment of *b* (e.g., 0°:5°:15° means that the values are 0°, 5°, 10°, and 15°).

[b]Red and NIR represent the parameters in the red and NIR bands.

Table 2. Quality screening for the MOD/MYD09GA dataset.

1-km QA		
	Cloud	Clear
	Cloud shadow	No
	Land water	Land
	Aerosol	Not high
	Cirrus	None or small
	Internal cloud	No
	Adjacent cloud	No
	Snow or Ice	No
500-m QC	Band quality	Highest quality

QA, quality assurance; QC, quality control.

50-km × 50-km region (100 × 100 pixels) located in North America (101°19′56″ to 100°24′30″W, 30°5′18″ to 30°30′18″N). The multiangle MODIS observations for 16 consecutive days of the 2 regions were used for approaches comparison (from July 9 to 24, 2019, for the first region, and from July 1 to 16, 2020, for the second region). The Landsat RGB (bands 4, 3, and 2) composite image (downloaded from https://glovis.usgs.gov/), terrain, and the number of available MODIS observations of the 2 regions are shown in Fig. 3.

Multiangle UAV measurements

Using UAVs to acquire pixel BRDF needs many multiangle observations, which requires long periods of good and stable atmospheric conditions. The kernel-driven model can model pixel BRDF using a small number of multiangle observations. In this paper, 3 UAV measurement datasets acquired over pixels of row crops (maize, sunflower, and wheat) were used to validate the ability of the DWLS approach in the BRDF construction. These UAV datasets, which were acquired from crops in the reproductive stage, have been previously used to evaluate the impact of reproductive organs on crop BRDF [52]. The 3 crop fields were located in Avignon, France (43.9°N, 4.9°E). A hexacopter UAV designed by Atechsys (http://atechsys.fr/) carrying the AIRPHEN multispectral camera (https://www.hiphen-plant.com/our-solutions/airphen/) was used for data acquisition. The camera had 6 spectral bands (450, 530, 570, 675, 730, and 850 nm). In this study, only the red (675 nm) and NIR (850 nm) bands were used. The UAV sampled 5 view zenith angles (VZAs) (0°, 15°, 30°, 45°, and 60°) for as many view azimuth angles (VAAs) as possible by flying along with 5 concentric circles. Meanwhile, encrypted observations were made in the hotspot direction during the measurement. In the original experiment, the UAV flew 3 times during the day, corresponding approximately to 30°, 45°, and 60° solar zenith angles (SZAs) over each pixel. The datasets with 30° SZA were used for the validation of DWLS. During the UAV flights, the sky was clear without clouds. There was a light wind during maize and sunflower acquisitions, while in the case of wheat, the wind was stronger, with however no severe degradation of the sampling scheme. The 3 datasets contain 200 (wheat), 102 (maize), and 280 (sunflower) available observations, respectively, which is enough for the validation of DWLS. More detailed information on these datasets can be found in [52].

Due to the difficulty of acquiring multiangle reflectance data using the UAV, the selected pixels are small and the corresponding terrains are flat. However, for small-scale pixels, the heterogeneity of pixels can be caused by the heterogeneous reflectance properties of the vegetation structure, especially for sunflowers. The mutual shielding of different parts of vegetation can also influence the BRDF of pixels. This also meets the validation needs of the DWLS approach. The aerial photos of these 3 pixels are given in Fig. 4.

Methods

Kernel-driven model and current inversion approach

The kernel-driven models provide a synthetic interpretation of the complex scattering mechanisms of land surfaces via the linear combination of the isotropic-scattering, volume-scattering, and geometric-optical kernels. The initial equation of the kernel-driven model is given by Roujean et al. [18] as:

$$r(\vartheta, \theta, \xi, \lambda) = f_{iso}(\lambda) K_{iso}(\vartheta, \theta, \xi)$$
$$+ f_{vol}(\lambda) K_{vol}(\vartheta, \theta, \xi) + f_{geo}(\lambda) K_{geo}(\vartheta, \theta, \xi) \tag{1}$$

where $r(\vartheta, \theta, \xi, \lambda)$ is the reflectance in the waveband λ, which is a function of the SZA ϑ, VZA θ, and relative azimuth angle ξ. $f_{iso}(\lambda)$, $f_{vol}(\lambda)$, and $f_{geo}(\lambda)$ are the weight components of the isotropic-scattering kernel $K_{iso}(\vartheta, \theta, \xi)$ (considered as 1), volume-scattering kernel $K_{vol}(\vartheta, \theta, \xi)$, and geometric-optical kernel $K_{geo}(\vartheta, \theta, \xi)$.

Given m reflectance observations $R_{(m \times 1)}$, the 3-parameter linear kernel-driven models expressed in Eq. 1 can be written in the following matrix form:
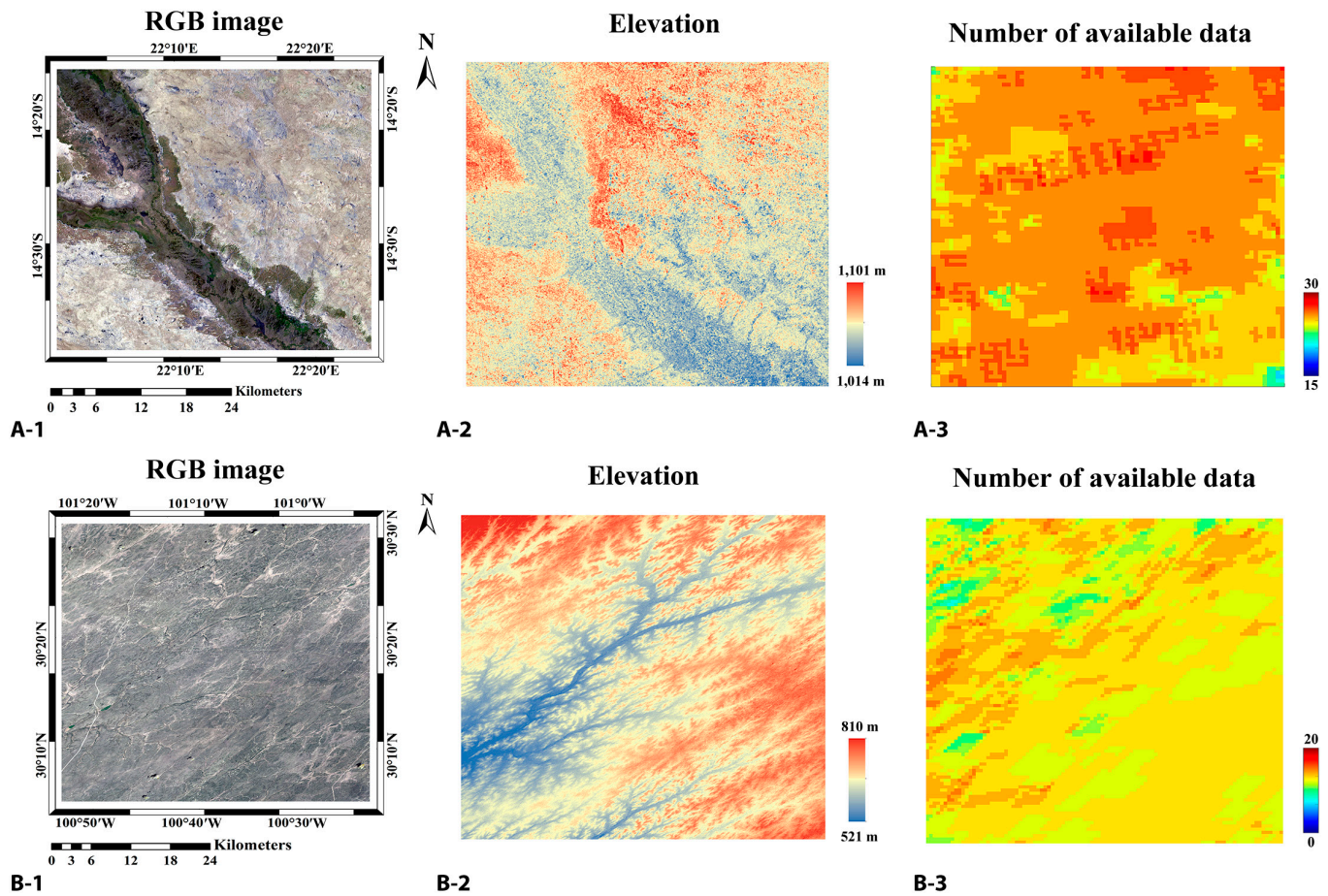
Fig. 3. The surface conditions and the number of available reflectance data for the study areas. (A-1) and (B-1) are the Landsat RGB images of the 2 regions; (A-2) and (B-2) are the terrain of the 2 regions; and (A-3) and (B-3) are the number of available observations from MODIS of the 2 regions.

$$R_{(m \times 1)} = K_{(m \times 3)} F_{(3 \times 1)} \tag{2}$$

where $R_{(m \times 1)}$ is the known observation vector with m different sun-sensor geometries. $K_{(m \times 3)}$ and $F_{(3 \times 1)}$ are the kernel matrix calculated using the known reflectances and the kernel coefficients vector to be derived. The cost function of the inverse problem can be written as the following matrix:

$$\left(R_{(m \times 1)} - K_{(m \times 3)} F_{(3 \times 1)} \right)^{\mathrm{T}} \Sigma^{-1}_{(m \times m)} \left(R_{(m \times 1)} - K_{(m \times 3)} F_{(3 \times 1)} \right) \tag{3}$$

where $\Sigma_{(m \times m)}$ is the covariance matrix of measurement errors, and $\Sigma^{-1}_{(m \times m)}$ is the inverse matrix of Σ. $\Sigma^{-1}_{(m \times m)}$ can be replaced with a weight matrix $W_{(m \times m)}$, which contains the weight of each observation:

$$\left(R_{(m \times 1)} - K_{(m \times 3)} F_{(3 \times 1)} \right)^{\mathrm{T}} W_{(m \times m)} \left(R_{(m \times 1)} - K_{(m \times 3)} F_{(3 \times 1)} \right) \tag{4}$$

The kernel coefficients vector can be calculated as:

$$F_{(3 \times 1)} = \left(K^{\mathrm{T}}_{(3 \times m)} W_{(m \times m)} K_{(m \times 3)} \right)^{-1} \left(K^{\mathrm{T}}_{(3 \times m)} W_{(m \times m)} R_{(m \times 1)} \right) \tag{5}$$

where $K^{\mathrm{T}}_{(3 \times m)}$ is the transpose of the kernel matrix. When $W_{(m \times m)}$ is set as a unit matrix $E_{(m \times m)}$, the coefficient matrix $F_{(3 \times 1)}$ and the reflectance to be predicted $r_{(n \times 1)}$ can be calculated as:

$$F_{(3 \times 1)} = \left(K^{\mathrm{T}}_{(3 \times m)} E_{(m \times m)} K_{(m \times 3)} \right)^{-1} \left(K^{\mathrm{T}}_{(3 \times m)} E_{(m \times m)} R_{(m \times 1)} \right) \tag{6}$$

$$r_{(n \times 1)} = k_{(n \times 3)} F_{(3 \times 1)} = k_{(n \times 3)} \left(K^{\mathrm{T}}_{(3 \times m)} E_{(m \times m)} K_{(m \times 3)} \right)^{-1}$$
$$\left(K^{\mathrm{T}}_{(3 \times m)} E_{(m \times m)} R_{(m \times 1)} \right) \tag{7}$$

where n is the number of reflectances to be predicted and $k_{(n \times 3)}$ is the kernel matrix of these reflectances, which can be calculated with their sun-sensor geometries. This approach is the OLS inversion approach commonly used for kernel-driven models currently.

Theoretical basis of the new-proposed DWLS approach

Equation 7 implies that all the observations are assigned the same weight to estimate the kernel coefficients, which kernel-driven models use to calculate the unknown reflectances in other directions. This means that all the known observations play the same role in predicting the reflectance in different directions when using the OLS approach. This may be acceptable for flat and homogeneous pixels. However, for rugged pixels, the upward, downward radiation and vegetation growth can be affected by topography [53,54]. On the other hand, each pixel can contain more than 1 component, especially for low-spatial-resolution pixels. Therefore, due to terrain and the mutual shielding of the component, it is difficult to observe the same objects from different directions in heterogeneous pixels
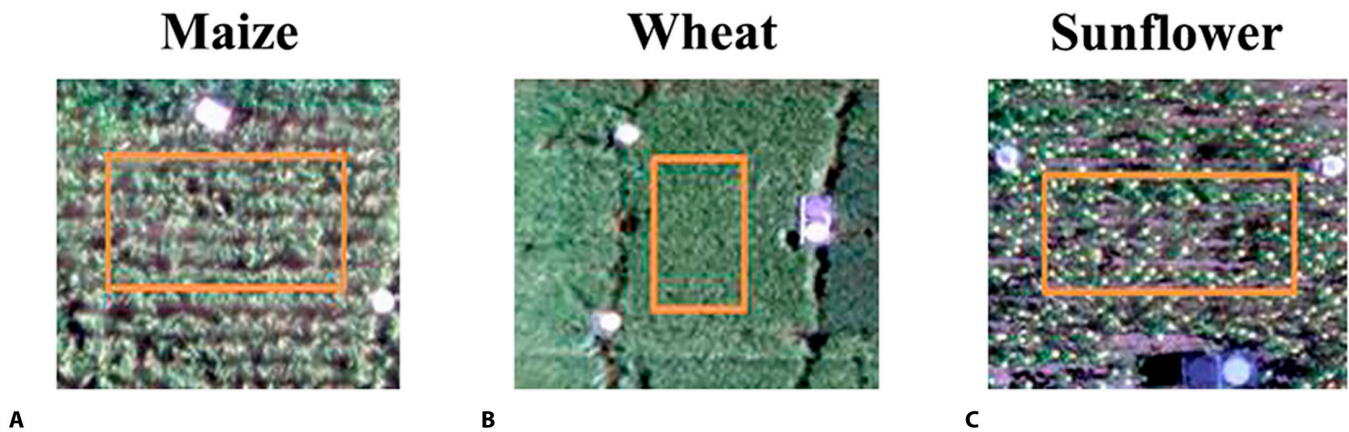
Maize   Wheat   Sunflower

A   **B**   **C**

Fig. 4. (A to C) Aerial photographs of the UAV data pixels where orange rectangles mark the areas where the data was acquired.

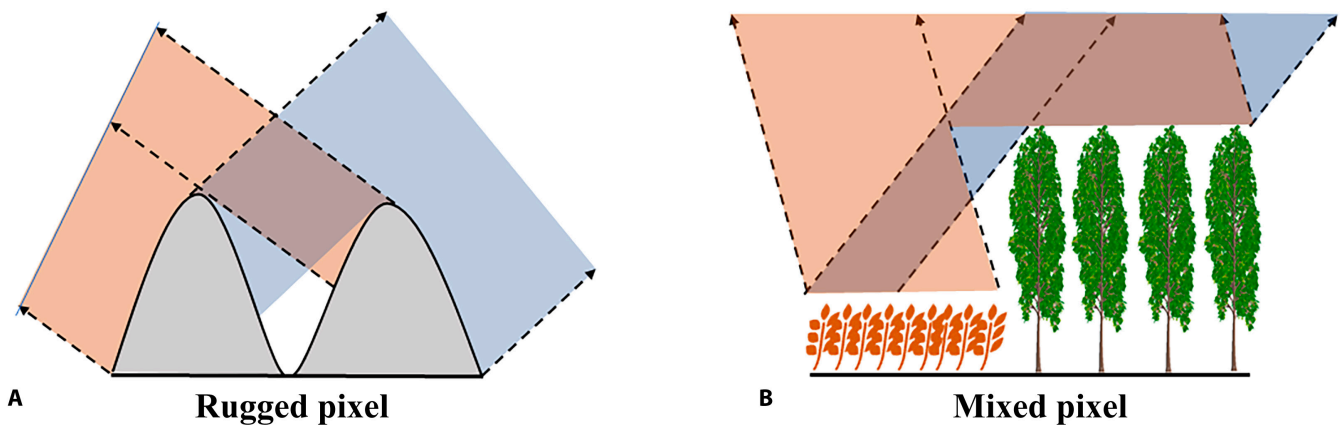**A**   **Rugged pixel**   **B**   **Mixed pixel**

Fig. 5. Differences in the observed objects in different directions due to terrain and objects' mutual shielding. Orange and blue areas represent 2 different directions. (A) Terrain shielding in a rugged pixel. (B) Component shielding in a mixed pixel.

(Fig. 5). We are more likely to observe the mostly same objects in the adjacent directions. In other words, the correlation between the reflectance in 2 directions decreases as the phase angle between the 2 directions increases.

As mentioned above, the role that the known observation in direction $\Omega_i(\theta_i,\varphi_i)$ can play in predicting the reflectance in direction $\Omega_j(\theta_j,\varphi_j)$ should be related to the included angle of the 2 directions, which can be expressed with the phase angle ζ_{ij}:

$$\zeta_{ij}=\arccos\left(\cos\theta_i\cos\theta_j+\sin\theta_i\sin\theta_j\cos\left(\varphi_i-\varphi_j\right)\right) \quad (8)$$

where θ_i and φ_i are the VZA and VAA of the i - th known reflectance in direction $\Omega_i(\theta_i,\varphi_i)$, and θ_j and φ_j are the VZA and VAA of the j - th reflectance to be predicted in direction $\Omega_j(\theta_j,\varphi_j)$, respectively. The direction that is adjacent to the direction to be predicted should have a larger weight, so an inverse angle distance weighting method can be used. The weight of the observation in direction $\Omega_i(\theta_i,\varphi_i)$ for the inversion of reflectance in direction $\Omega_j(\theta_j,\varphi_j)$ can be expressed as:

$$w_{ij}=\frac{1}{\zeta_{ij}} \quad (9)$$

However, the sun position has a significant effect on the pixel BRDF, and the above method is only applicable to the case where the sun positions are similar. Therefore, a correction term ς_{ij} can be added to the weighting function, which can be expressed as:

$$\varsigma_{ij}=\arccos\left(\cos\vartheta_i\cos\vartheta_j+\sin\vartheta_i\sin\vartheta_j\cos\left(\phi_i-\phi_j\right)\right) \quad (10)$$

where ϑ_i and ϕ_i are the SZA and solar azimuth angle (SAA) of the i - th known reflectance in direction $\Omega_i(\vartheta_i,\phi_i,\theta_i,\varphi_i)$, and ϑ_j and ϕ_j are the SZA and SAA of the j - th reflectance to be predicted in direction $\Omega_j(\vartheta_j,\phi_j,\theta_j,\varphi_j)$. Finally, the weighting function can be written as:

$$w_{ij}=\frac{1}{\zeta_{ij}+\varsigma_{ij}} \quad (11)$$

In this way, when the difference in the sun direction of known and unknown reflectances is large, the effect of observation direction differences on the weights of the known reflectances becomes smaller. This means that the DWLS approach degenerates toward OLS when the sun direction differs significantly. Then, the weight matrix for the reflectance to be predicted can be expressed as:

$$W_j = diag\left(w_{1j}, w_{2j}, \cdots, w_{ij}, \cdots w_{mj}\right) = \begin{bmatrix} w_{1j} & 0 & \cdots & 0 & \cdots & 0 \\ 0 & w_{2j} & \cdots & 0 & \cdots & 0 \\ \vdots & \vdots & \ddots & 0 & \cdots & 0 \\ 0 & 0 & 0 & w_{ij} & \cdots & 0 \\ \vdots & \vdots & \vdots & \vdots & \ddots & 0 \\ 0 & 0 & 0 & 0 & 0 & w_{mj} \end{bmatrix}$$
(12)

Substituting Eq. 12 into Eq. 5, we obtain the kernel coefficient matrix for the j-th reflectance to be predicted:

$$F_{j(3\times1)} = \left(K^{\mathrm{T}}_{(3\times m)} W_{j(m\times m)} K_{(m\times3)}\right)^{-1} \left(K^{\mathrm{T}}_{(3\times m)} W_{j(m\times m)} R_{(m\times1)}\right)$$
(13)

The full coefficient matrix can be expressed as:

$$f_{(3\times n)} = \begin{bmatrix} F_1 & F_2 & \cdots & F_j & \cdots & F_n \end{bmatrix}$$
(14)

Then, we can calculate the reflectance matrix:

$$r_{(n\times n)} = k_{(n\times3)} f_{(3\times n)} = k_{(n\times3)} \begin{bmatrix} F_1 & F_2 & \cdots & F_j & \cdots & F_n \end{bmatrix}_{(3\times n)}$$
(15)

where $k_{(n\times3)}$ is the kernel matrix of the reflectances to be predicted. The values on the main diagonal of the matrix $r_{(n\times n)}$ are the reflectances that need to be predicted. These mean that a set of kernel coefficients is generated by the DWLS approach for each predicted direction. The contribution of the input reflectances to the predicted direction is reevaluated in each calculation of the kernel coefficients.

As shown in Fig. 6, the DWLS approach differs from OLS in that it calculates the weights of the known reflectances based on geometric information of the unknown and known reflectances.

Approach analysis and assessment
Comparison between the OLS and DWLS approaches
The kernel-driven models can reconstruct the pixel BRDF with multiangle observations using the OLS or DWLS approach. Among the various kernel-driven models, the RTLSR model is widely used due to its good fitting ability, consisting of the RossThick volume-scattering kernel and the LiSparseReciprocal geometric-optical kernel [19]. It has been adopted in an operational algorithm for the MODIS BRDF/Albedo product [22,23]. In this study, the RTLSR model will be used to compare the OLS and DWLS inversion approaches. We used simulated data to evaluate the DWLS approach and tested its performance in MODIS observation reconstruction and UAV BRDF construction.

For the RTLSR model, which is a 3-parameter kernel-driven model, both the inversion approaches theoretically require at least 3 known reflectances and their sun-sensor geometries as input data to predict the reflectances in other directions. However, additional well-distributed observations are needed to ensure inversion accuracy in practical application. For simulated and UAV-measured reflectances, we used 12 uniformly distributed reflectances as input data to predict other reflectances and compared the performance of the OLS and DWLS approaches. Because of the fewer available observations, for the satellite data, 8 uniformly distributed reflectances from all available Terra and Aqua MODIS observations were selected for the

inversion. We also used observations from Terra MODIS to predict those from Aqua MODIS and compared the fitting ability of the 2 approaches. The root mean square error (RMSE), coefficient of multiple determination (R^2), and optimization rate (OR) were used to compare the OLS and DWLS approaches quantitatively. They can be calculated by the following equations:

$$\mathrm{RMSE} = \sqrt{\frac{1}{n-1} \sum_{i=1}^{n} (y_i - x_i)^2}$$

$$R^2 = \frac{\left[\sum_{i=1}^{n} (y_i - \bar{y})(x_i - \bar{x})\right]^2}{\sum_{i=1}^{n} (y_i - \bar{y})^2 \times (x_i - \bar{x})^2}$$
(16)

$$\mathrm{OR} = \frac{\mathrm{RMSE}_{\mathrm{OLS}} - \mathrm{RMSE}_{\mathrm{DWLS}}}{\mathrm{RMSE}_{\mathrm{OLS}}} \times 100\%$$

where x_i is the simulated or observed reflectance, y_i is the predicted reflectance by the OLS or DWLS approach, and n is the number of reflectances to be predicted. $\mathrm{RMSE}_{\mathrm{OLS}}$ and $\mathrm{RMSE}_{\mathrm{DWLS}}$ are the RMSE of the OLS and DWLS approaches, respectively. When $\mathrm{OR} > 0$, it means that the DWLS approach exhibits higher accuracy than OLS. The input reflectances are not involved in the calculation of these evaluation indicators, and the input data are the same for both approaches.

Performance analysis of the DWLS approach
Measured reflectances may be affected by instrument noise, aerosols, data preprocessing, and other factors, and these uncertainties are inevitable. The DWLS approach assigns different
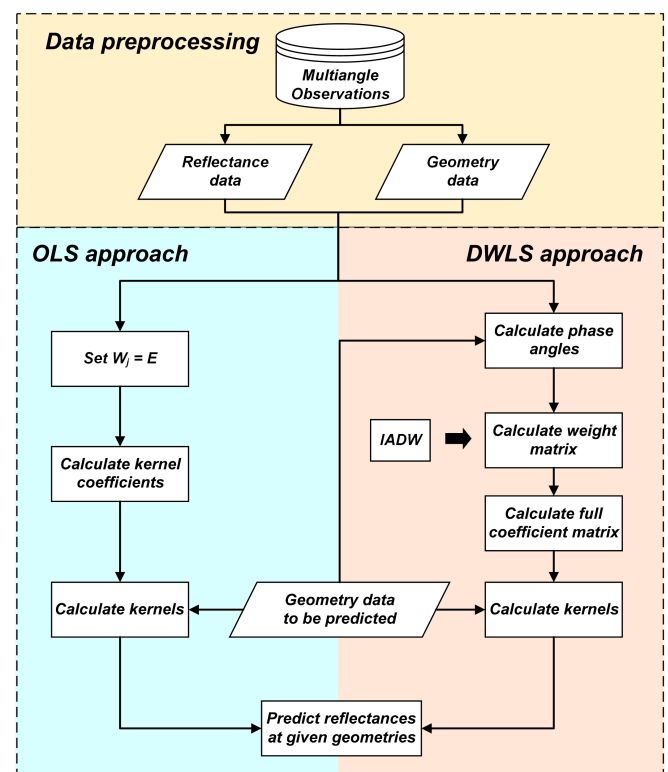

Fig. 6. Comparison of the inversion process of the OLS and DWLS approaches. W_j is the weight matrix for j-th reflectance to be predicted. E is the unit matrix. IADW, inverse angle distance weighting method.

weights to known observations in the inversion process, which may introduce more uncertainty than the OLS approach. Therefore, it is necessary to perform an uncertainty analysis for DWLS to understand this approach better. In this paper, we analyzed the influence of observation uncertainty and angle sampling distribution on the inversion accuracy of the DWLS approach. For this reason, 2 experiments were designed based on the simulated data:

Experiment I: Effect of observation uncertainty. We assume that the observation uncertainty e follows the normal distribution $N(0, \sigma^2)$, which can be expressed as:

$$e \sim N\left(0, \sigma^2\right) \tag{17}$$

where σ is the standard deviation (SD) that represents the fluctuation of the observation uncertainties. The measured reflectance R_m should follow the normal distribution $N(\mu, \sigma^2)$

$$R_m \sim N\left(\mu, \sigma^2\right) \tag{18}$$

where μ is the mean reflectance that presents the true value simulated in this experiment R_s. In addition, σ can be set to $p \cdot R_s$, where p is a scaling factor satisfying $p = 0\%, 2\%, \ldots,$ 50% in this experiment. Thus, we obtain:

$$R_m \sim N\left(R_s, \left(p \cdot R_s\right)^2\right), \quad p = 0\%, 2\%, \ldots, 50\% \tag{19}$$

Then, for different p, we generated 10,000 simulated reflectances R_m satisfying Eq. 19 as input data for the OLS and DWLS approaches to calculate the RMSE. Meanwhile, we performed the same operation for all sampled directions and calculated the mean RMSE and its SD, which can represent the mean fitting residuals and fluctuation range of the 2 approaches, respectively. The results of this experiment are shown in Uncertainty and sensitivity analysis.

Experiment II: Effect of angle sampling distribution. Undoubtedly, more widely distributed angle samples are beneficial to BRDF inversion [55]. However, for satellite data, the directions of available observations may be limited due to orbiting configuration and the data quality. Therefore, the fitting abilities of the OLS and DWLS approaches were explored with limited angle sampling. We designed 4 angle sampling methods (Fig. 7). Method I is an approximation of the full Terra and Aqua MODIS sampling capabilities for a site [55], and the others were used to

simulate the absence of observations in some angles. The geometries of the simulated data shown in Fig. 7 are used as inputs to predict reflectances in other directions. Then, the inversion accuracies of the OLS and DWLS approaches using these 4 angle sampling methods were compared. The results are discussed in Influence of the angle sampling distribution.

Results

Evaluation based on simulated data

A comparison of the inverted BRDF shapes using the OLS and DWLS approaches is given in Fig. 8. Due to the inherent symmetry of the kernels of the RTLSR model, the BRDF shapes inverted by the OLS approach are strictly symmetric about the solar principal plane (Fig. 8A-2 and B-2). However, the shapes of the simulated BRDF do not exhibit this characteristic due to topographic effects. Especially in the NIR band, there is a big difference between the simulated and OLS inverted BRDF shapes. In contrast, the DWLS approach reconstructs the BRDF of this pixel more accurately in both the red and NIR bands. As shown in Fig. 8A-4 and B-4, BRFs inverted by DWLS are closer to the simulated BRFs compared to those inverted by OLS. The RMSE of OLS are 0.0029 and 0.0154 in the red and NIR bands, whereas those of the DWLS approach are 0.0020 and 0.0100. In contrast, the DWLS approach shows a larger R^2 than OLS. The R^2 of the OLS approach are 0.9174 and 0.7636, but those of DWLS can reach 0.9604 and 0.9028 in the 2 bands. Comparing the R^2, we can find that both the OLS and DWLS approaches have better performance in the red band than in the NIR band. This is because the soil is treated as Lambertian in the simulation, and the heterogeneity caused by the rugged terrain is mainly expressed by the reflection contribution of the vegetation, which is larger in the NIR band. These results show that the DWLS approach can better overcome interferences caused by complex terrain.

Figure 9 compared the inversion accuracy of the OLS and DWLS approaches over all rugged pixels at different SZAs. For the red band, the DWLS approach shows a relatively narrower RMSE distribution at all SZAs, whereas a larger and more dispersed RMSE was noted in the OLS approach. The maximum RMSE of the DWLS approach are 0.0053, 0.0051, 0.0029, 0.0051, and 0.0057 when SZA = 0°, 15°, 30°, 45°, and 60°, respectively, whereas the maximum RMSE of the OLS approach are 0.0063, 0.0063, 0.0044, 0.0064, and 0.0106. Similar results
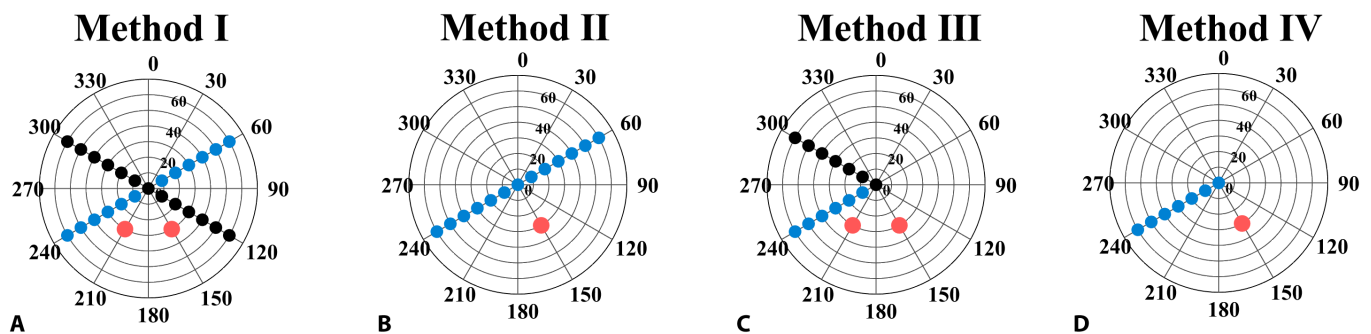
Fig. 7. (A to D) Four different angle sampling methods used for analyzing the effect of observation distribution on inversion accuracy. The blue and black dots represent the directions that were adopted as input data for the RTLSR model and were used to simulate the observation directions of Terra and Aqua MODIS, respectively. The red dots show the simulated solar position for Terra (SAA = 150°) and Aqua (SAA = 210°), respectively. Concentric rings denote 10° increments of VZA. Radial lines represent 30° increments of VAA.
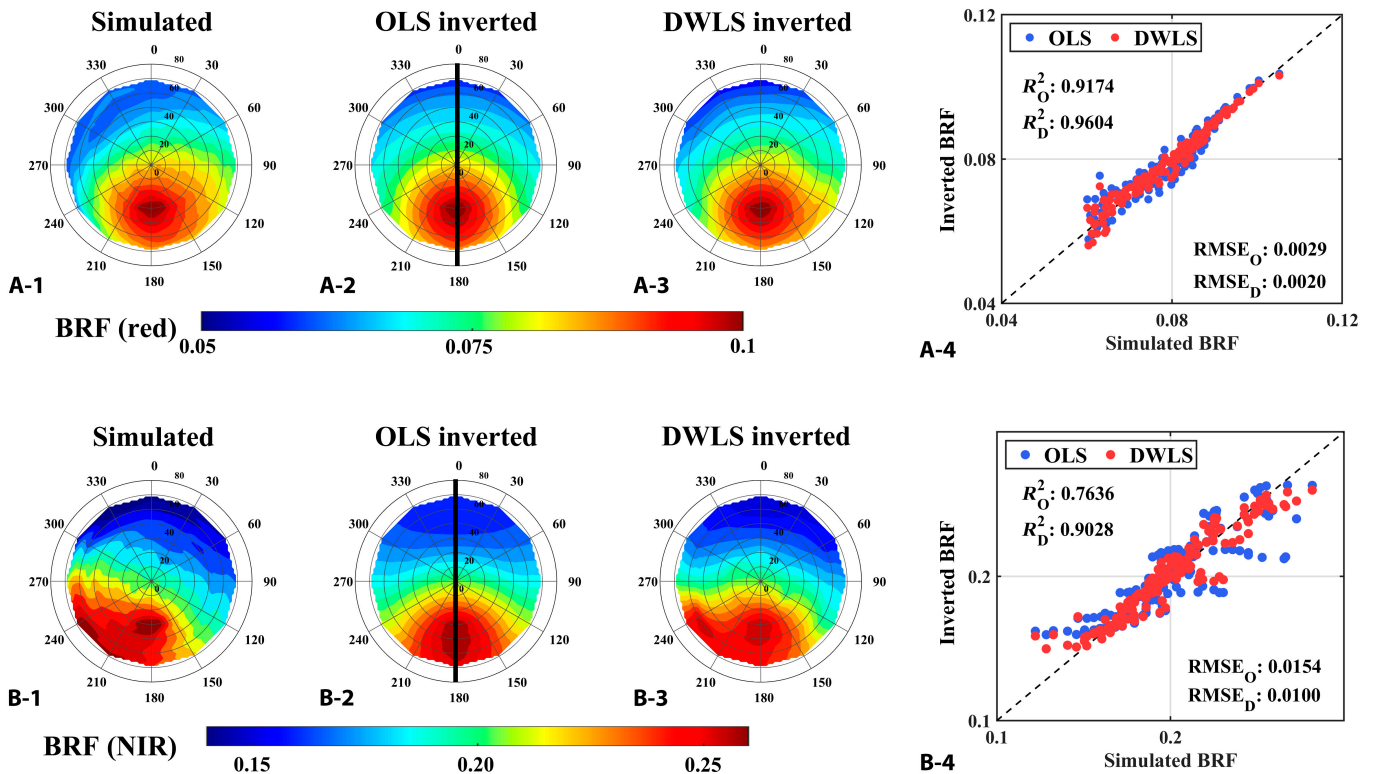
Fig. 8. Comparison of the inverted BRDF shapes in a single pixel (marked in Fig. 1) between the OLS and DWLS approaches in the red (A) and NIR (B) bands using simulated datasets. (A-1) and (B-1) are the simulated BRDF shapes, (A-2) and (B-2) are the BRDF shapes inverted by the OLS approach, and (A-3) and (B-3) are the BRDF shapes inverted by the DWLS approach. The color bars represent BRF values. (A-4) and (B-4) compare the inversion accuracy of the OLS and DWLS approaches. The black lines in (A-2) and (B-2) mark the solar principal plane.
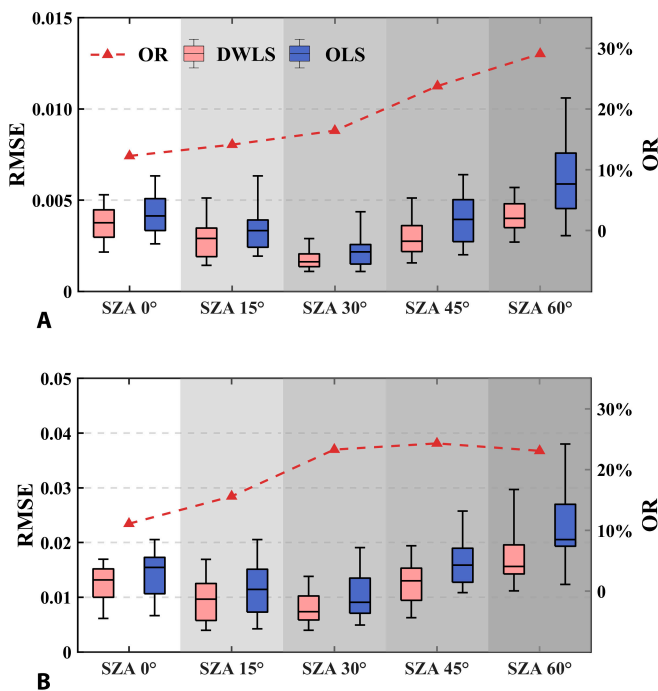

Fig. 9. Accuracy comparison of the OLS and DWLS approaches over simulated rugged pixels at different SZAs in the red (A) and NIR (B) bands. The boxplots show the RMSE distribution for the DWLS and OLS approaches. The lines are the mean ORs for different SZAs. The different shades of background color represent the different SZAs.

are also shown in the NIR band. For the NIR band, the maximum RMSE of the DWLS is 0.0297 when SZA = 60°, whereas that of the OLS approach is 0.0380. These mean that the DWLS approach shows better performance at all SZAs in the 2 bands. Comparing the mean OR in the 2 bands, we can find that OR exhibits a positive correlation with SZA. Meanwhile, the RMSE of the 2 approaches show a trend of decreasing and then increasing. This is due to the combined effect of the decrease in reflectance values and the poor fitting ability of the RTLSR model at large SZA [56]. In summary, the DWLS approach achieves higher inversion accuracy over these rugged pixels.

The inversion results of the DWLS and OLS approaches at SZA = 30° over the mixed and control pixels in the red band are compared in Fig. 10. The results for the NIR band are given in Fig. S1. For the control pixel (Pixel A), its simulated BRDF shape is typical and regular. In Fig. 10A-3 and A-4, both BRDF shapes inverted by the OLS and DWLS approaches are similar to the simulated BRDF shape. The R^2 between BRFs inverted by the 2 approaches and simulated BRFs are 0.9102 and 0.9230, respectively, which means that OLS and DWLS both perform well on this homogeneous pixel. However, the BRDF shapes of the mixed pixels (Pixels B to E) are more complex. Especially for Pixels B and C, due to the symmetry of the kernels, the OLS approach cannot restore their BRDF shapes accurately. This suggests that the fitting ability of the RTLSR model is affected by the clumping and occlusion of objects within the pixels. The DWLS approach performs better in Pixels B to E, where it accurately captures their BRDF characteristics. The R^2 of the OLS approach are 0.4535, 0.4762, 0.8868, and 0.4476 in Pixels B to
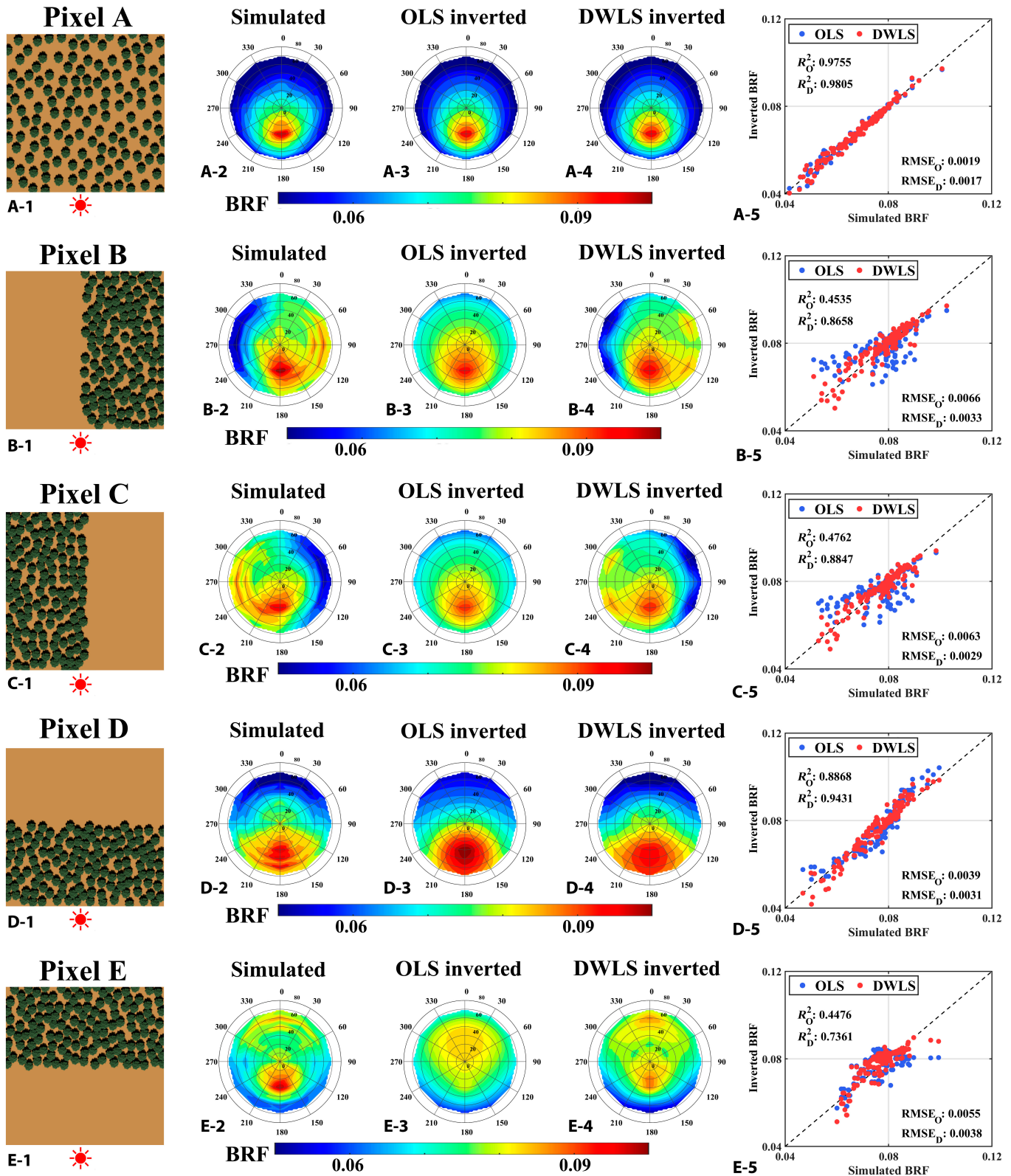
Fig. 10. Comparison of inversion results of the OLS and DWLS approaches over simulated control and mixed pixels in the red band (SZA = 30°). (A) are the inversion results of the control pixels; (B) to (E) are the inversion results of the 4 mixed pixels; (1) 3-D scenes of these pixels. (2) to (4) are BRDF shapes from simulation, OLS, and DWLS, respectively; (5) are the comparisons of the inversion accuracy of the OLS and DWLS approaches.

E, whereas those of the DWLS approach are 0.8658, 0.8847, 0.9431, and 0.7361, respectively. The RMSEs of the 2 approaches over the 4 pixels show similar patterns. The results in the NIR band are similar. These results indicate that the DWLS approach can better fit the BRDF for these mixed pixels than the OLS approach.

Similarly, the performance of the 2 approaches was compared over mixed pixels when the SZA changes. The RMSE and R^2 of the OLS and DWLS approaches are given in Fig. 11 for Pixels A to E and SZA = 0° to 60°. Overall, we can see that the solid shapes representing the DWLS approach are concentrated in the upper left corner of the 2 panels. On the contrary, the hollow shapes representing the OLS approach appear more often in the lower right corner of the panels, which indicates that the DWLS approach showed overall lower RMSE and higher R^2 compared with the OLS approach. The mean RMSE of the OLS and DWLS approaches are 0.0064 and 0.0049 in the red band and 0.0175 and 0.0158 in the NIR band, respectively. The mean R^2 of OLS are 0.5466 and 0.6663 in the red and NIR bands, respectively, while the mean R^2 of DWLS both reached above 0.7 in the 2 bands. Through specific comparison of the same scene, we can find that the solid points with the same color and shape always appear on the upper left of the hollow points. This means that the DWLS approach can invert the BRDF more accurately. Similar to Fig. 9, both approaches exhibit lower fitting residuals at SZA = 30°. This should also be due to the reflectance value and the characteristics of the RTLSR model.

Performance in MODIS observation reconstruction
Observation reconstruction for Terra and Aqua MODIS observations

Figure 12 compares the observation reconstruction accuracy of the OLS and DWLS approaches when Terra and Aqua MODIS data are both used in the study areas. In Fig. 12, we can find that for both study regions, the RMSE of the DWLS

approach are smaller in both the red and NIR bands, and the ORs of most pixels are positive. For the first study region, statistics show that 93.84% of the pixels have a positive OR in the red band and 87.05% in the NIR band. The OR reached a maximum of 78.74% and 77.14% in the red and NIR bands, respectively. Meanwhile, the mean RMSE are 0.0116 and 0.0076 for the OLS and DWLS approaches in the red band and 0.0191 and 0.0139 in the NIR band, respectively. For the second study regions, the DWLS approach performs better over about 91.16% and 96.20% of pixels in the red and NIR bands, respectively. The mean RMSE are 0.0230 and 0.0195 for the OLS and DWLS approaches in the red band and are 0.0282 and 0.0204 for the NIR band, respectively. By comparing the distribution of OR and RMSE of the 2 approaches, we can find that in pixels where DWLS performs poorly, the OLS approach also shows large RMSE. This may be due to limitations in the distribution or uncertainty of observations. In general, the DWLS approach performs better in the area with complex surface conditions than the OLS approach.

The scatterplots in Fig. 13 represent the degree of agreement between the reflectances from OLS and DWLS and from MODIS observations in the study regions. The fitting lines of reflectances inverted by the 2 approaches and MODIS are also given in Fig. 13. It is clear that the fitting lines for OLS show a stronger deviation from the 1:1 line compared to those of DWLS, which implies that the reflectances inverted by the DWLS approach have a stronger agreement with MODIS observations. For the first study region (Fig. 13A and B), The R^2 of OLS are 0.7678 and 0.7770 in the red and NIR bands, respectively, which are smaller than 0.9160 and 0.8897 of the DWLS approach. The RMSE of the 2 approaches show similar results. The DWLS approach reduces the RMSE of the OLS approach from 0.0102 to 0.0061 in the red band and from 0.0169 to 0.0118 in the NIR band. Similar results can be found in Fig. 13C and D. These results suggest that the reflectances from DWLS agree better with the MODIS observations than those inverted by OLS.
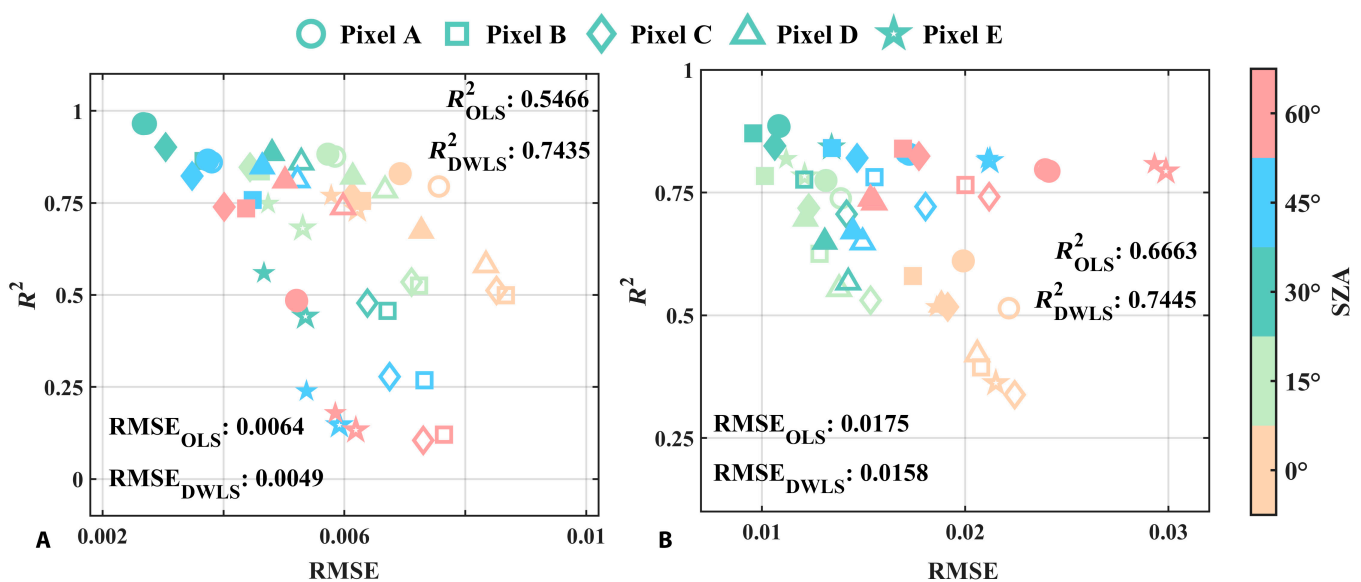
Fig. 11. Accuracy comparison of the OLS (hollow shapes) and DWLS (solid shapes) approaches over simulated mixed pixels at different SZAs in the red (A) and NIR (B) bands. The different shapes of the points represent different mixed pixels (Pixels A to E), and the colors represent different SZAs. The hollow and solid shapes represent the results from the OLS and DWLS approaches, respectively.
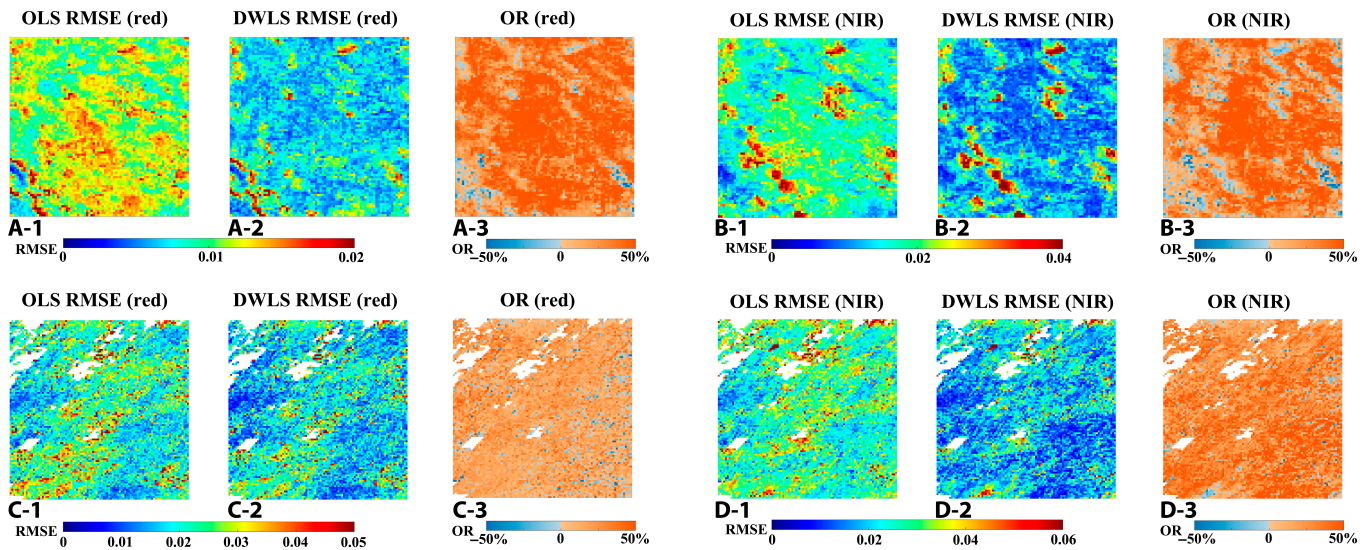
Fig. 12. Comparison of inversion results of the OLS and DWLS approaches using Terra and Aqua MODIS data for 2 study regions in the red and NIR bands. (A) and (B) are the results of the first study region in the red and NIR bands, respectively. (C) and (D) are the results of the second study region in the red and NIR bands, respectively. (1) and (2) are the RMSE of the OLS and DWLS approaches, respectively. The color bars of (1) and (2) represent the RMSE values from small (blue) to large (red). (3) Distribution of OR. The color bars of (3) represent the OR values from negative (blue) to positive (orange).
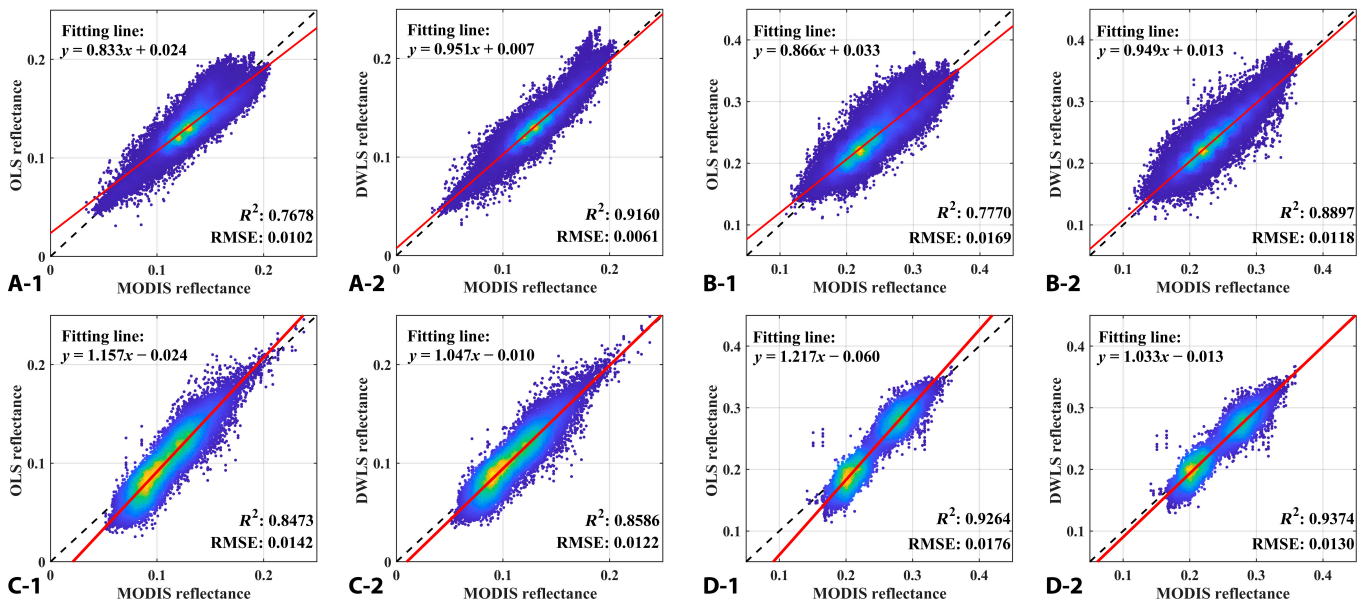

Fig. 13. Comparison of the reflectances inverted by the OLS and DWLS approaches in the 2 study regions. (A) and (B) show the results for the first study region in the red and NIR bands, respectively; (C) and (D) show the results for the second study region in the red and NIR bands, respectively; (1) are reflectance comparisons from OLS and MODIS; (2) are reflectance comparisons from DWLS and MODIS. The red lines are the fitting lines. The point density colors range from low (blue) to high (yellow).

Predicting Aqua MODIS observations using Terra MODIS observations

The performance of the OLS and DWLS approaches using Terra observations to predict Aqua observations is compared in Fig. 14. These histograms show the distribution of RMSE and R^2 of the 2 approaches for all pixels of the 2 study regions. In Fig. 14, we can find that the RMSE of DWLS are smaller compared to those of the OLS approach in the red band, and the difference is more evident for the NIR band. For the first study region, statistics show that the DWLS approach exhibits a

smaller RMSE in 75.41% of the pixels in the red band and 79.44% for the NIR band. This indicates that the DWLS approach has an advantage over the OLS approach in predicting reflectance in more pixels. Meanwhile, in R^2 histograms of the 2 approaches in red and NIR bands, the values of DWLS are larger than those of the OLS approach. The CDF (cumulative distribution function) lines visually compare the statistical patterns of the indicators of the 2 approaches: the CDF lines of DWLS RMSE reach 1 earlier (when the RMSE are smaller) in both red and NIR bands, and the CDF lines of DWLS R^2 reach 1 later
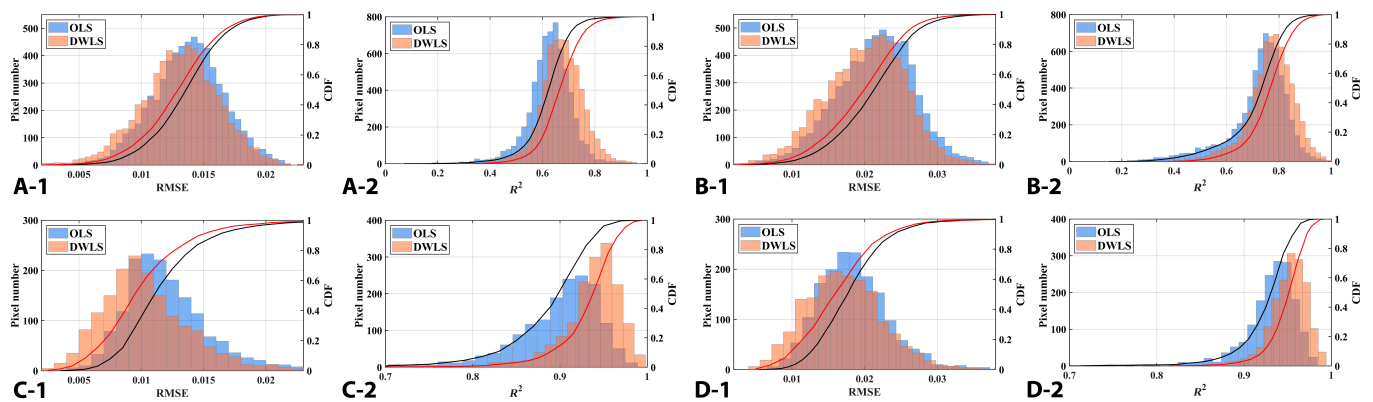
Fig. 14. Histogram of the accuracy of the OLS and DWLS approaches using Terra observations (MOD09GA) to predict Aqua observations (MYD09GA). (A) and (B) are the results for the first study region in the red and NIR bands, respectively; (C) and (D) are the results for the second study region in the red and NIR bands, respectively; (1) are RMSE histograms; (2) are R^2 histograms. The red and black lines are the CDF of the DWLS and OLS approaches, respectively.

Table 3. The results of UAV data validation.

Pixels	Red				NIR			
	RMSE		R^2		RMSE		R^2	
	OLS	DWLS	OLS	DWLS	OLS	DWLS	OLS	DWLS
Wheat	0.0073	0.0054	0.9049	0.9475	0.0115	0.0088	0.9454	0.9696
Maize	0.0045	0.0025	0.5720	0.9071	0.0219	0.0138	0.8035	0.9320
Sunflower	0.0049	0.0041	0.7893	0.8173	0.0163	0.0137	0.6165	0.7450

(when the R^2 are larger). Similar results can also be found for the second study regions. These results suggest that the DWLS approach shows higher accuracy in more pixels and stronger robustness.

Performance in BRDF construction using UAV observations

The ability of the DWLS approach in BRDF construction was validated by 3 UAV measurement datasets. Table 3 gives the inversion results of the OLS and DWLS approaches, and Fig. 15 shows a comparison of inverted BRDF and their accuracy by the 2 approaches over the maize pixel. The results in Table 3 show that the inversion accuracies of the DWLS approach are higher for 3 row crop pixels compared to the OLS approach. In both red and NIR bands, the RMSE of DWLS are smaller and the R^2 are closer to 1. Particularly in the maize pixel, the RMSE of the OLS approach are 0.0045 and 0.0219, whereas those of DWLS are 0.0025 and 0.0138 in the red and NIR bands, respectively. The R^2 of the DWLS approach are both larger than 0.9 in the 2 bands, whereas those for the OLS approach are 0.5720 and 0.8035, respectively. For the sunflower pixel, although both of the R^2 for the 2 approaches are less than 0.9 in the red and NIR bands, the DWLS approach performs better. The RMSE of the 2 approaches suggest the same results. The OLS and DWLS approaches both show good performance in the wheat pixels, their R^2 both larger than 0.9. This should be due to the

more homogeneous canopy cover in wheat compared to maize and sunflower pixels. We then compared the inverted BRDF shapes by the OLS and DWLS approaches in the maize pixel with the observed BRDF shape in Fig. 15. It can be found that there is a larger difference between the inverted BRDF shape by the OLS approach and the observed BRDF shape compared to that from the DWLS approach. Figure 15A-3 and B-3 illustrates the frequency distribution of the δBRF in the red and NIR bands. By comparing the frequency fitting curves of the δBRF for the 2 approaches, it can be seen that the δBRF of DWLS are more concentrated around 0 compared to those of the OLS approach, which means that the BRFs inverted by the DWLS approach have smaller deviations. These comparisons show that the DWLS approach provides a more accurate construction of BRDF than the OLS approach.

Uncertainty of the DWLS approach
Uncertainty and sensitivity analysis

The results presented in Fig. 16 correspond to Experiment I described in Performance analysis of the DWLS approach. We used the generated reflectances satisfying Eq. 19 with different uncertainties as input data for the RTLSR model to compare the sensitivities of the OLS and DWLS approaches to observation uncertainty. The mean RMSEs of the 2 approaches are represented by the colored lines in Fig. 16. It is clear that the mean RMSEs of OLS and DWLS increase with increasing observation
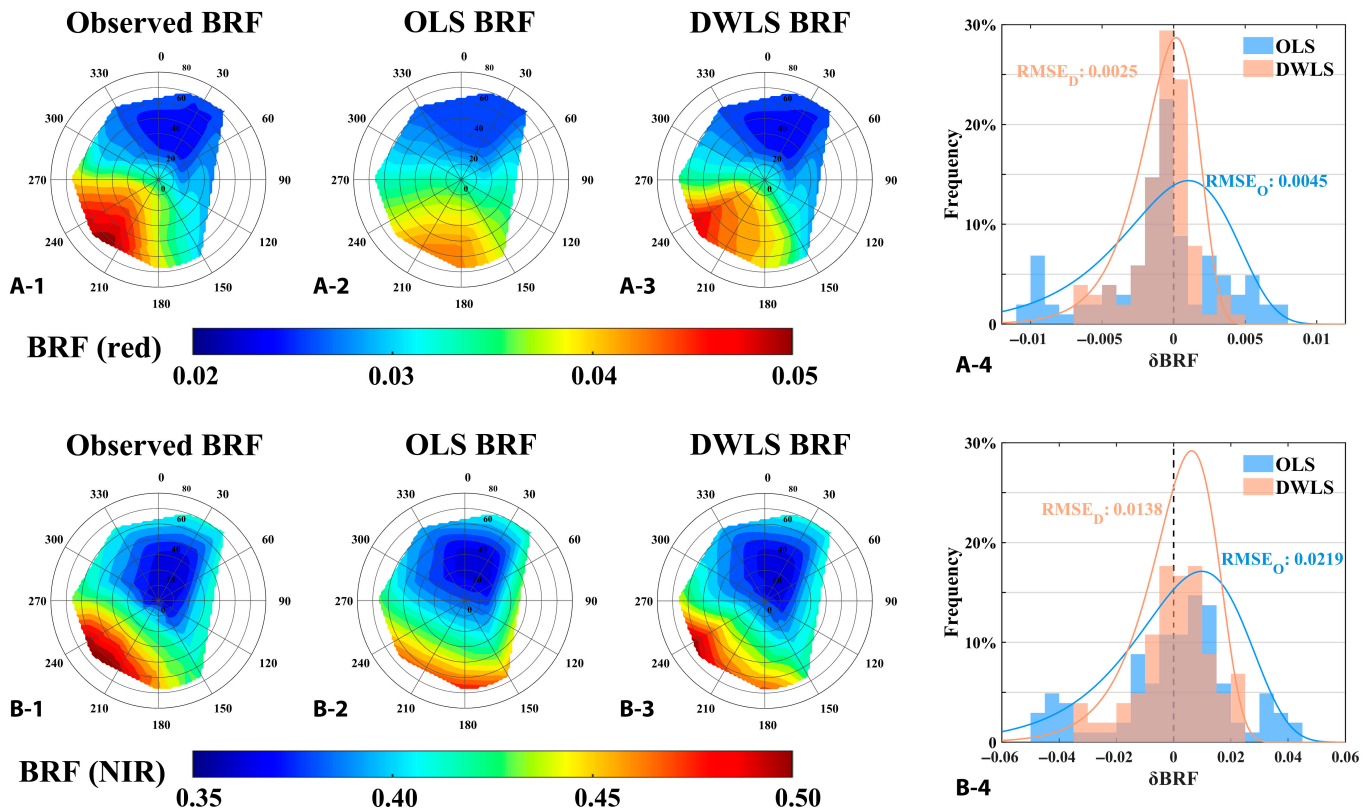
Fig. 15. Comparison of the inversion results using the UAV measured data over the maize pixel between the OLS and DWLS approaches in the red (A) and NIR (B) bands. (A-1) and (B-1) are the measured BRDF shapes. (A-2) and (B-2) are the BRDF shapes inverted by the OLS approaches. (A-3) and (B-3) are the BRDF shapes inverted by the DWLS approaches. The color bars represent BRF values. (A-4) and (B-4) are the comparisons of the inversion accuracies of the OLS and DWLS approaches. δBRF represents the absolute deviation of BRF. The colored dashed lines are the frequency fitting curves of δBRF.
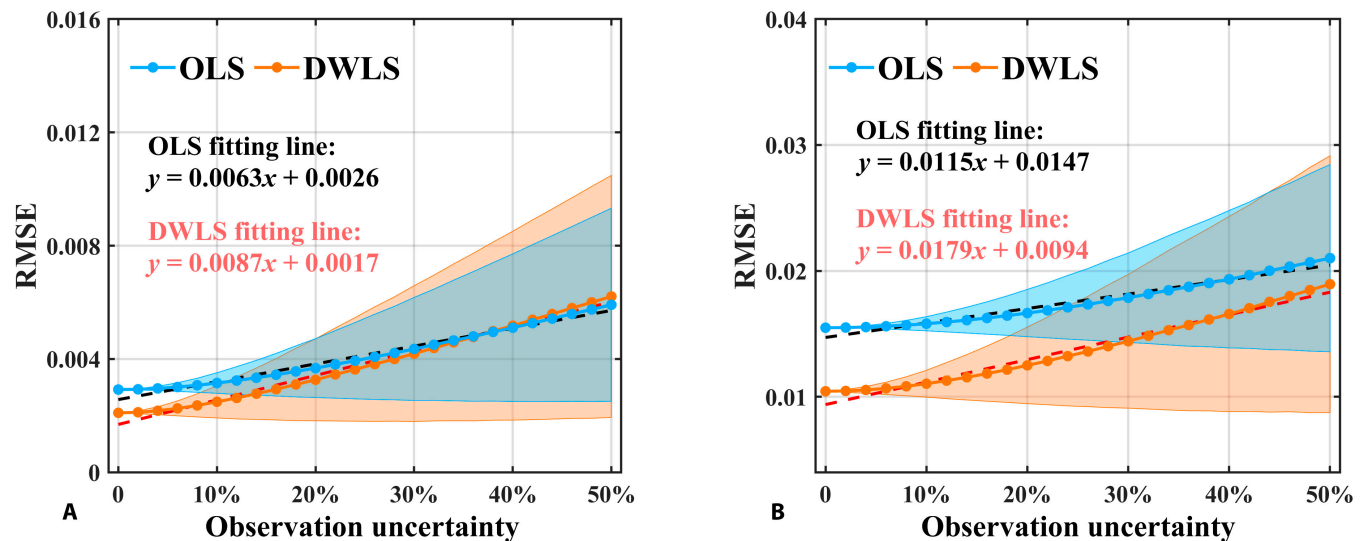

Fig. 16. Comparison of uncertainty sensitivity between the OLS and DWLS approaches in the red (A) and NIR (B) bands. The colored lines are the mean RMSEs of the 2 approaches. The black and red dashed lines are the fitting lines of the mean RMSE of OLS and DWLS, respectively. The blue and orange shaded areas indicate the RMSE SDs of the OLS and DWLS approaches.

uncertainty in both bands, and the mean RMSE of the DWLS approach increases faster. This can also be seen from their fitting lines: the gradients of the OLS fitting line are 0.0063 and 0.0115 in the red and NIR bands, respectively, whereas those of the DWLS fitting lines are 0.0087 and 0.0179. The RMSE SDs of

the 2 approaches, represented by shaded backgrounds, show the fluctuation range of their RMSE, and the DWLS approach exhibits a larger SD than OLS. This suggests that the DWLS approach is more susceptible to observation uncertainty than the OLS approach. Nevertheless, the DWLS approach still
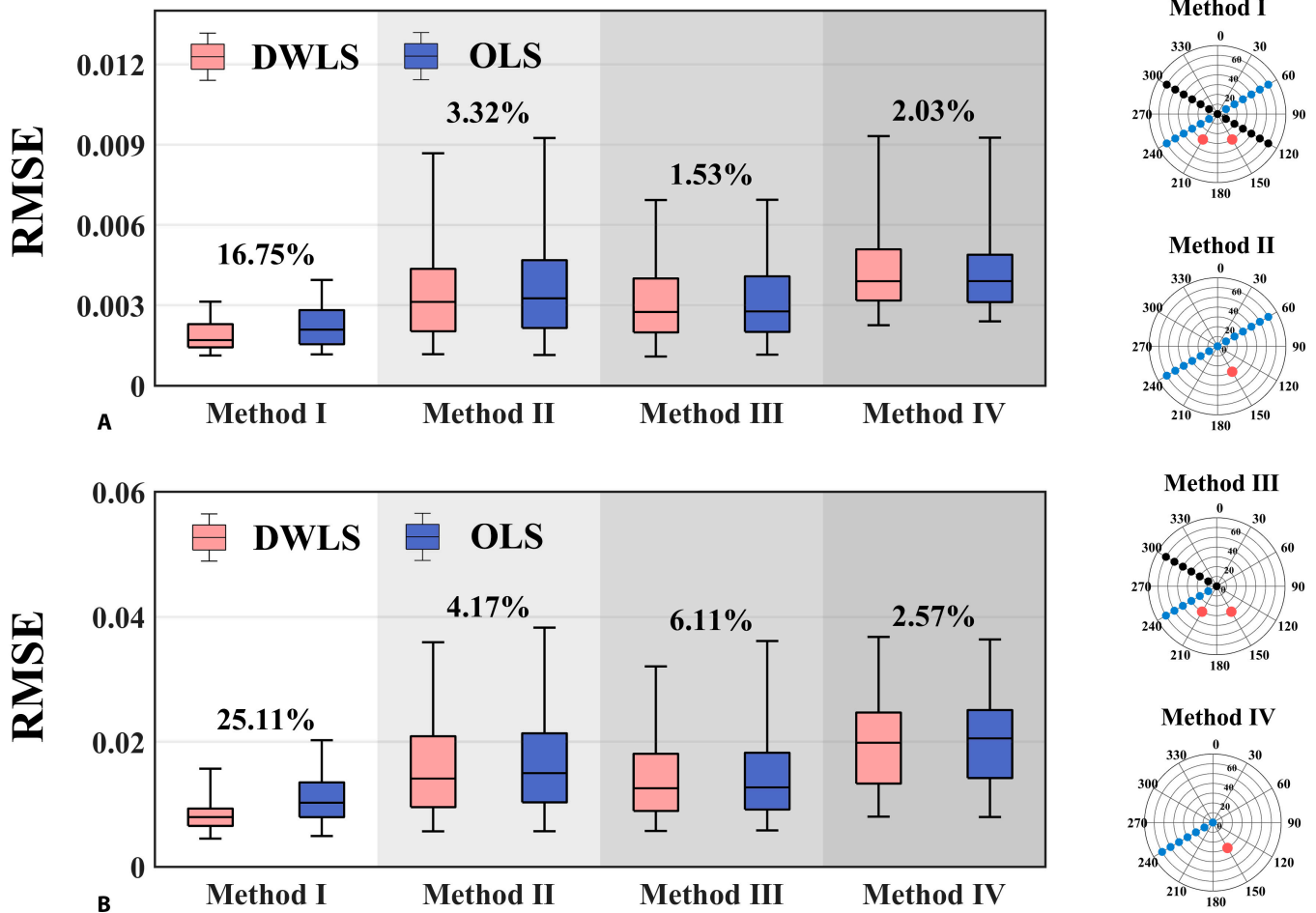
Fig. 17. Comparison of the inversion accuracies of the OLS and DWLS approaches using different angle sampling methods. (A) and (B) represent the results in the red and NIR bands, respectively. The marked numbers above boxes are ORs of different sampling methods calculated by the mean RMSE. The 4 angle sampling methods are given in the polar plots on the right panel.

shows higher inversion accuracy when the observation uncertainty is small.

Influence of the angle sampling distribution

Satellite measurements may be affected by clouds and aerosols, resulting in a direction concentration of available reflectances. We compared the inversion capability of the OLS and DWLS approaches under different angle sampling conditions (Fig. 17). These results correspond to Experiment II described in Performance analysis of the DWLS approach.

For Method I, both the OLS and DWLS approaches show small and narrow RMSE distribution. However, for Methods II, III, and IV, the RMSEs of both the OLS and DWLS approaches are larger and more discrete due to missing observations. These results mean that both the OLS and DWLS approaches are affected by the observation distribution, and their inversion accuracies decrease as the observation distribution is limited. By comparing the OR of the 4 sampling methods, we can find that OR can reach about 20% in the red and NIR bands for Method I with ideal observations. They decrease to less than 10% as the distribution of the observation becomes more concentrated. This indicates that the optimization effect of the DWLS approach compared to OLS is also influenced by the observation distribution.

Discussion

Characteristics of the DWLS approach

The kernels are key to the physical meaning of the kernel-driven models. The approximate physical basis of the kernels substantially constrains the possible BRDF shapes in unobserved regions of the viewing and illumination hemisphere. However, most kernels are highly hypothetical and more suitable for homogeneous pixels, which is a root cause of the challenge of original kernel-driven models over heterogeneous pixels [56,57]. Therefore, up to now, scholars have been working to improve the fitting ability of the kernel-driven model by improving new kernels through physical methods [40–43]. However, the inversion approach is also critical for the kernel-driven models, because they are a kind of semiempirical model.

The inversion process of kernel-driven models is a linear weighting of the BRDF decomposition of the pixels into 3 ideal situations (isotropic-scattering, volume-scattering, and geometric-optical). The kernel coefficients calculated using the known multiangle reflectances are the weight values of the 3 scenes. The OLS approach assigns the same weight to all known observations in the BRDF inversion to solve for the kernel coefficients of the pixels. This means that the OLS approach decomposes the pixel into a fixed weighted combination of 3 ideal radiative

transfer scenes. This may be acceptable for flat and homogeneous pixels but not for heterogeneous pixels; observing the pixel from a different perspective may result in a completely different scene. Heterogeneity has become a critical factor affecting the pixel BRDF. The radiative transfer process within the heterogeneous pixels can no longer be accurately described by a fixed weighted combination. The DWLS approach dynamically calculates the weights of known observations using their geometry information to invert the BRDF of the heterogeneous pixels, which makes better use of structure information within the pixels carried by the multiangle observations. Therefore, the DWLS approach performs better and obtains more accurate BRDF inversions over heterogeneous pixels than OLS.

However, uncertainty is inevitable in observations and challenges the performance of the proposed DWLS approach. We found that the DWLS approach is more sensitive to input uncertainties than the OLS approach, as verified in Uncertainty and sensitivity analysis, which limits the application of the DWLS approach. Fortunately, Zeng et al. [58] have already proposed a changing-weight iterative BRDF inversion algorithm that can adjust the weight of each observation according to its noise level and effectively improve the robustness of BRDF inversion. This algorithm can be used to remove observations with large uncertainties before BRDF inversion using the DWLS approach. In Influence of the angle sampling distribution, the influence of the available observation distribution on the DWLS approach was also explored. It is worth noting that the DWLS approach outperforms OLS in all cases. Meanwhile, as the distribution of known observations becomes wider, the DWLS approach exhibits a higher optimization effect.

In addition, the DWLS approach, similar to the OLS approach, can be used in combination with all kernel-driven models. Since the introduction of the kernel-driven models, there has been considerable effect to improve them and develop many new kernels or forms of the kernel-driven models over more than 2 decades [56]. Therefore, the performance of the DWLS approach in combination with other kernel-driven models is also expected.

In summary, the DWLS approach has several characteristics: (a) The DWLS approach can take advantage of multiangle reflectances for more accurate BRDF modeling without any additional input data. (b) This approach is more sensitive to large uncertainties in observation than OLS. (c) The observation distribution affects the optimization effect of DWLS. When the observation distribution tends to be concentrated, the accuracy of DWLS and OLS approaches tends to be similar. (d) The DWLS approach can be used with other kernel-driven models. Considering these characteristics, we believe that the DWLS approach can be a good choice when the kernel-driven models are applied to heterogeneous pixels.

Application of the DWLS approach and future works

The DWLS and OLS approaches, as inversion methods, can be combined with the kernel-driven models and used to: (a) invert pixel's BRDF; (b) reconstruct missing satellite observations; (c) correct bidirectional effects and calculate nadir BRDF-adjusted reflectance (NBAR); and (d) estimate surface albedo, and other parameters. In this paper, we compared the ability of OLS and DWLS approaches to invert BRDF and reconstruct the missing MODIS observations for heterogeneous pixels. The results show that the DWLS approach is more advantageous over heterogeneous pixels. Compared with the OLS approach and

other models, it can more accurately invert the BRDF by using multiangle observations without additional input data, which facilitates the accurate construction of pixel BRDF using UAV observations. We made no effort to estimate NBAR and albedo in this paper. Theoretically, the DWLS approach should be more robust for the NBAR calculation because it is less susceptible to the interference of reflectance with large VZA, which is vulnerable to heterogeneity within the heterogeneous pixels. However, for albedo estimation, we think that the DWLS approach may not exhibit a noticeable optimization effect. This is because the reflectance with large VZA contributes less to the estimation of albedo and there may be complementarity in different orientations.

Therefore, there are still some aspects of our study that need to be further explored. Firstly, we focused on the development and analysis of the approach and did not quantitatively compare the DWLS approach with other BRDF models for heterogeneous pixels. The practical application of DWLS for estimating NBAR and albedo also needs to be investigated. Secondly, although the DWLS approach does not require additional input data, it is more sensitive to observation uncertainty than OLS. How the influence of observations with large uncertainties on the DWLS approach can be reduced needs further exploration. Finally, only the RTLSR model is used for the evaluation and analysis of the DWLS approach in this paper. The performance of DWLS when combined with other kernel-driven models is also worth exploring. These issues are also crucial for the wide application of the DWLS approach and will be our future work.

Conclusion

In this study, we tried to improve the fitting ability of the kernel-driven models over heterogeneous pixels by changing the inversion approach. Then, we proposed the DWLS method to address this issue. The simulated, satellite-, and UAV-measured multiangle data were used to compare the DWLS approach and the traditional OLS approach quantitatively. In the evaluation based on the simulated data, the results show that the DWLS approach is more suitable for heterogeneous pixels than the OLS approach. Meanwhile, the DWLS approach exhibits higher accuracy and robustness in MODIS observation reconstruction and BRDF construction using UAV observations, even though it still shows higher sensitivity to observation uncertainty. In summary, the developed DWLS approach based on the kernel-driven models can capture BRDF characteristics more accurately over heterogeneous pixels. We believe that it can be a better choice when the kernel-driven models are applied to satellite observation reconstruction or BRDF construction by UAV observations. In future studies, the DWLS approach has the potential to be extended to estimate land and biophysical parameters (e.g., NBAR and leaf area index) over heterogeneous landscapes.

Acknowledgments

the discussion and revised the submitted manuscript. **Competing interests:** The authors declare that they have no competing interests.

Data Availability

The DEM data for simulation and MODIS data can be obtained from https://lpdaac.usgs.gov/. The UAV data can be obtained from the authors on request.

Supplementary Materials

Fig. S1
NOMENCLATURE

References

1. Nicodemus FE, Richmond JC, Hsia JJ, Ginsberg IW, Limperis T. *Geometrical considerations and nomenclature for reflectance*. Final Report National Bureau of Standards; 1977.

2. Schaepman-Strub G, Schaepman ME, Painter TH, Dangel S, Martonchik JV. Reflectance quantities in optical remote sensing—Definitions and case studies. *Remote Sens Environ*. 2006;103(1):27–42.

3. Knyazikhin Y, Martonchik JV, Myneni RB, Diner DJ, Running SW. Synergistic algorithm for estimating vegetation canopy leaf area index and fraction of absorbed photosynthetically active radiation from MODIS and MISR data. *J Geophys Res Atmos*. 1998;103(D24):32257–32275.

4. Liang S, Strahler AH, Walthall C. Retrieval of land surface albedo from satellite observations: A simulation study. *J Appl Meteorol Climatol*. 1999;38(6):712–725.

5. Xu B, Park T, Yan K, Chen C, Zeng Y, Song W, Yin G, Li J, Liu Q, Knyazikhin Y, et al. Analysis of Global LAI/FPAR products from VIIRS and MODIS sensors for spatio-temporal consistency and uncertainty from 2012–2016. *Forests*. 2018;9(2):73.

6. Yan K, Park T, Yan G, Liu Z, Yang B, Chen C, Nemani RR, Knyazikhin Y, Myneni RB. Evaluation of MODIS LAI/FPAR Product Collection 6. Part 2: Validation and Intercomparison. *Remote Sens*. 2016;8(6):460.

7. Hintz M, Lennartz-Sassinek S, Liu S, Shao Y. Quantification of land-surface heterogeneity via entropy spectrum method. *J Geophys Res Atmos*. 2014;119(14):8764–8777.

8. Jacob F, Weiss M. Mapping biophysical variables from solar and thermal infrared remote sensing: Focus on agricultural landscapes with spatial heterogeneity. *IEEE Geosci Remote Sens Lett*. 2014;11(10):1844–1848.

9. Zeng Y, Li J, Liu Q, Li L, Xu B, Yin G, Peng J. A sampling strategy for remotely sensed LAI product validation over heterogeneous land surfaces. *IEEE J Sel Top Appl Earth Obs Remote Sens*. 2014;7(7):3128–3142.

10. Yin G, Li J, Liu Q, Li L, Zeng Y, Xu B, Yang L, Zhao J. Improving leaf area index retrieval over heterogeneous surface by integrating textural and contextual information: A case study in the Heihe River Basin. *IEEE Geosci Remote Sens Lett*. 2015;12(2):359–363.

11. Zeng Y, Li J, Liu Q, Huete AR, Yin G, Xu B, Fan W, Zhao J, Yan K, Mu X. A radiative transfer model for heterogeneous agro-forestry scenarios. *IEEE Trans Geosci Remote Sens*. 2016;54(8):4613–4628.

12. Yu W, Li J, Liu Q, Zeng Y, Zhao J, Xu B, Yin G. Global land cover heterogeneity characteristics at moderate resolution for mixed pixel modeling and inversion. *Remote Sens*. 2018;10(6):856.

13. Suits GH. The calculation of the directional reflectance of a vegetative canopy. *Remote Sens Environ*. 1971;2:117–125.

14. Li X, Strahler AH. Geometric-optical bidirectional reflectance modeling of the discrete crown vegetation canopy: Effect of crown shape and mutual shadowing. *IEEE Trans Geosci Remote Sens*. 1992;30(2):276–292.

15. Walthall CL, Norman JM, Welles JM, Campbell G, Blad BL. Simple equation to approximate the bidirectional reflectance from vegetative canopies and bare soil surfaces. *Appl Opt*. 1985;24(3):383–387.

16. Koukal T, Atzberger C, Schneider W. Evaluation of semi-empirical BRDF models inverted against multi-angle data from a digital airborne frame camera for enhancing forest type classification. *Remote Sens Environ*. 2014;151:27–43.

17. Martonchik JV, Diner DJ, Pinty B, Verstraete MM, Myneni RB, Knyazikhin Y, Gordon HR. Determination of land and ocean reflective, radiative, and biophysical properties using multiangle imaging. *IEEE Trans Geosci Remote Sens*. 1998;36(4):1266–1281.

18. Roujean J-L, Leroy M, Deschamps P-Y. A bidirectional reflectance model of the Earth's surface for the correction of remote sensing data. *J Geophys Res*. 1992;97(D18):20455.

19. Wanner W, Li X, Strahler AH. On the derivation of kernels for kernel-driven models of bidirectional reflectance. *J Geophys Res*. 1995;100(D10):21077.

20. Lucht W, Schaaf CB, Strahler AH. An algorithm for the retrieval of albedo from space using semiempirical BRDF models. *IEEE Trans Geosci Remote Sens*. 2000;38(2):977–998.

21. Wanner W, Strahler AH, Hu B, Lewis P, Muller JP, Li X, Schaaf CLB, Barnsley MJ. Global retrieval of bidirectional reflectance and albedo over land from EOS MODIS and MISR data: Theory and algorithm. *J Geophys Res Atmos*. 1997;102(D14):17143–17161.

22. Schaaf CB, Gao F, Strahler AH, Lucht W, Li X, Tsang T, Strugnell NC, Zhang X, Jin Y, Muller JP, et al. First operational BRDF, albedo nadir reflectance products from MODIS. *Remote Sens Environ*. 2002;83(1–2):135–148.

23. Schaaf CB, Liu J, Gao F, Strahler AH. MODIS albedo and reflectance anisotropy products from Aqua and Terra. In: Ramachandran B, Justice C, Abrams M, editors. *Land remote sensing and global environmental change: NASA's Earth Observing System and the science of ASTER and MODIS*. London (UK): Springer-Verlag; 2011. p. 873.

24. Wang Z, Schaaf CB, Sun Q, Shuai Y, Román MO. Capturing rapid land surface dynamics with Collection V006 MODIS BRDF/NBAR/Albedo (MCD43) products. *Remote Sens Environ*. 2018;207:50–64.

25. Deschamps P-Y, Breon FM, Leroy M, Podaire A, Bricaud A, Buriez JC, Seze G. The POLDER mission: Instrument characteristics and scientific objectives. *IEEE Trans Geosci Remote Sens*. 1994;32(3):598–615.

26. Bicheron P, Leroy M. Bidirectional reflectance distribution function signatures of major biomes observed from space. *J Geophys Res Atmos*. 2000;105(D21):26669–26681.

27. Bacour C, Bréon F-M. Variability of biome reflectance directional signatures as seen by POLDER. *Remote Sens Environ*. 2005;98(1):80–95.

28. Li X, Gao F, Chen L, Strahler AH. Derivation and validation of a new kernel for kernel-driven BRDF models. *Remote Sens Earth Sci Ocean Sea Ice Appl*. 1999;3868:368–379.

29. Gao F, Li X, Strahler A, Schaaf C. Evaluation of the Li transit kernel for BRDF modeling. *Remote Sens Rev*. 2000;19(1–4):205–224.

30. Maignan F, Bréon F-M, Lacaze R. Bidirectional reflectance of Earth targets: Evaluation of analytical models using a large set of spaceborne measurements with emphasis on the Hot Spot. *Remote Sens Environ*. 2004;90(2):210–220.

31. Jiao Z, Schaaf CB, Dong Y, Román M, Hill MJ, Chen JM, Wang Z, Zhang H, Saenz E, Poudyal R, et al. A method for improving hotspot directional signatures in BRDF models used for MODIS. *Remote Sens Environ*. 2016;186:135–151.

32. Dong Y, Jiao Z, Cui L, Zhang H, Zhang X, Yin S, Ding A, Chang Y, Xie R, Guo J. Assessment of the hotspot effect for the PROSAIL model with POLDER hotspot observations based on the hotspot-enhanced Kernel-Driven BRDF model. *IEEE Trans Geosci Remote Sens*. 2019;57(10):8048–8064.

33. Jiao Z, Dong Y, Li X. An approach to improve hot spot effect for the MODIS BRDF/Albedo algorithm. Paper presented at: IEEE: Proceedings of the 2013 IEEE International Geoscience and Remote Sensing Symposium - IGARSS; 2013 Jul 21–26; Melbourne, Australia.

34. Hao D, Zeng Y, Qiu H, Biriukova K, Celesti M, Migliavacca M, Rossini M, Asrar GR, Chen M. Practical approaches for normalizing directional solar-induced fluorescence to a standard viewing geometry. *Remote Sens Environ*. 2021;255:112171.

35. Cao B, Roujean J-L, Gastellu-Etchegorry J-P, Liu Q, Du Y, Lagouarde J-P, Huang H, Li H, Bian Z, Hu T, et al. A general framework of kernel-driven modeling in the thermal infrared domain. *Remote Sens Environ*. 2021;252:112157.

36. Hu B, Lucht W, Li X, Strahler AH. Validation of kernel-driven semiempirical models for the surface bidirectional reflectance distribution function of land surfaces. *Remote Sens Environ*. 1997;62(3):201–214.

37. Hu B, Wanner W, Li X, Strahler AH. Validation of kernel-driven semiempirical BRDF models for application to MODIS/MISR data. Paper presented at: IGARSS'96 1996 International Geoscience and Remote Sensing Symposium; 1996 May 31–31; Lincoln, NE.

38. Huang X, Jiao Z, Dong Y, Zhang H, Li X. Analysis of BRDF and albedo retrieved by kernel-driven models using field measurements. *IEEE J Sel Top Appl Earth Obs Remote Sens*. 2012;6(1):149–161.

39. Matsuoka M, Takagi M, Akatsuka S, Honda R, Nonomura A, Moriya H, Yoshioka H. Bidirectional reflectance modeling of the geostationary sensor HIMAWARI-8/AHI using a kernel-driven BRDF model. Paper presented at: ISPRS Annals of the Photogrammetry, Remote Sensing and Spatial Information Sciences; 2016 Jul 12–19; Prague, Czech Republic.

40. Yan K, Li H, Song W, Tong Y, Hao D, Zeng Y, Mu X, Yan G, Fang Y, Myneni RB, et al. Extending a linear kernel-driven BRDF model to realistically simulate reflectance anisotropy over rugged terrain. *IEEE Trans Geosci Remote Sens*. 2021;60:Article 4401816.

41. Wu S, Wen J, Xiao Q, Liu Q, Hao D, Lin X, You D. Derivation of kernel functions for kernel-driven reflectance model over sloping terrain. *IEEE J Sel Top Appl Earth Obs Remote Sens*. 2019;12(2):396–409.

42. Hao D, Wen J, Xiao Q, You D, Tang Y. An improved topography-coupled kernel-driven model for land surface anisotropic reflectance. *IEEE Trans Geosci Remote Sens*. 2020;58(4):2833–2847.

43. Kizel F, Vidro Y. Bidirectional reflectance distribution function (BRDF) of mixed pixels. *Int Arch Photogramm Remote Sens Spatial Inf Sci*. 2021;XLIII-B3-2021:195–200.

44. Qi J, Xie D, Guo D, Yan G. A large-scale emulation system for realistic three-dimensional (3-D) forest simulation. *IEEE J Sel Top Appl Earth Obs Remote Sens*. 2017;10(11):4834–4843.

45. Qi J, Xie D, Yin T, Yan G, Gastellu-Etchegorry JP, Li L, Zhang W, Mu X, Norford LK. LESS: LargE-Scale remote sensing data and image simulation framework over heterogeneous 3D scenes. *Remote Sens Environ*. 2019;221:695–706.

46. North PRJ. Three-dimensional forest light interaction model using a Monte Carlo method. *IEEE Trans Geosci Remote Sens*. 1996;34(4):946–956.

47. Govaerts YM, Verstraete MM. Raytran: A Monte Carlo ray-tracing model to compute light scattering in three-dimensional heterogeneous media. *IEEE Trans Geosci Remote Sens*. 1998;36(2):493–505.

48. Leblanc SG, Bicheron P, Chen JM, Leroy M, Cihlar J. Investigation of directional reflectance in boreal forests with an improved four-scale model and airborne POLDER data. *IEEE Trans Geosci Remote Sens*. 1999;37(3):1396–1414.

49. Chen JM, Blanken PD, Black TA, Guilbeault M, Chen S. Radiation regime and canopy architecture in a boreal aspen forest. *Agric For Meteorol*. 1997;86(1):107–125.

50. Yan K, Gao S, Chi H, Qi J, Song W, Tong Y, Mu X, Yan G. Evaluation of the vegetation-index-based dimidiate pixel model for fractional vegetation cover estimation. *IEEE Trans Geosci Remote Sens*. 2022;60:Article 4400514.

51. Wolfe RE, Roy DP, Vermote E. MODIS land data storage, gridding, and compositing methodology: Level 2 grid. *IEEE Trans Geosci Remote Sens*. 1998;36(4):1324–1338.

52. Li W, Jiang J, Weiss M, Madec S, Tison F, Philippe B, Comar A, Baret F. Impact of the reproductive organs on crop BRDF as observed from a UAV. *Remote Sens Environ*. 2021;259:Article 112433.

53. Yan G, Tong Y, Yan K, Mu X, Chu Q, Zhou Y, Liu Y, Qi J, Li L, Zeng Y, et al. Temporal extrapolation of daily downward shortwave radiation over cloud-free rugged terrains. Part 1: Analysis of topographic effects. *IEEE Trans Geosci Remote Sens*. 2018;56(11):6375–6394.

54. Hwang T, Song C, Vose JM, Band LE. Topography-mediated controls on local vegetation phenology estimated from MODIS vegetation index. *Landsc Ecol*. 2011;26(4):541–556.

55. Barnsley MJ, Strahler AH, Morris KP, Muller J. Sampling the surface bidirectional reflectance distribution function (BRDF): 1. Evaluation of current and future satellite sensors. *Remote Sens Rev*. 1994;8(4):271–311.

56. Li H, Yan K, Gao S, Song W, Mu X. Revisiting the performance of the kernel-driven BRDF model using filtered high-quality POLDER observations. *Forests*. 2022;13(3):Article 3.

57. Dong Y, Jiao Z, Zhang H, Bai D, Zhang X, Li Y, He D. A visualization tool for the kernel-driven model with improved ability in data analysis and kernel assessment. *Comput Geosci*. 2016;95:1–10.

58. Zeng Y, Li J, Liu Q, Huete AR, Xu B, Yin G, Zhao J, Yang L, Fan W, Wu S, et al. An iterative BRDF/NDVI inversion algorithm based on a posteriori variance estimation of observation errors. *IEEE Trans Geosci Remote Sens*. 2016;54(11):6481–6496.